

# Material Matters™

VOLUME 17 • NUMBER 1

## Special Issue

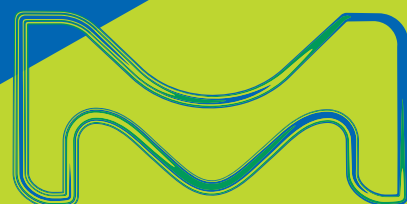
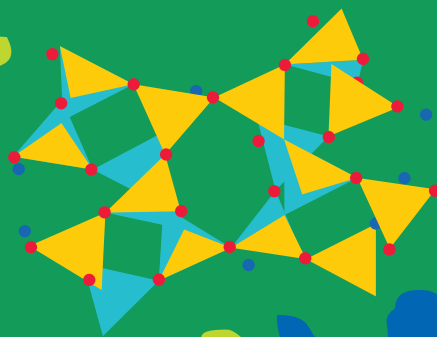
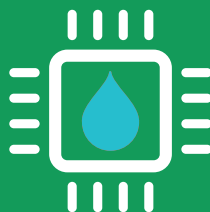
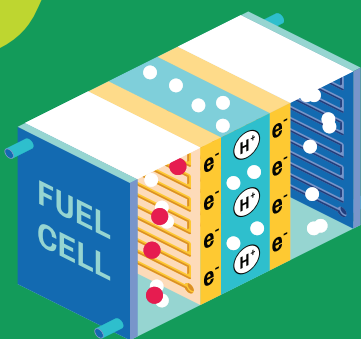
Featuring Cutting-edge Research from South Korea

PGM and PGM-free Catalysts for Polymer Electrolyte Membrane Fuel Cells

Sol-Gel Derived Siloxane-Encapsulated Luminescent Nanocrystal Composites for Optoelectronics and Display

Poly(2-isopropyl-2-oxazoline)-based Multimodal Stimuli-responsive Functional Materials

Phyllosilicate Clay Minerals: Principles and Applications



## Introduction



**Taryn L. Fuhrman-Hall, M.B.A.**  
Product Manager -  
Materials Science  
and Material Matters  
Coordinator

Welcome to the first issue of *Material Matters*™ for 2022, a special edition, focusing on some of the exciting research happening in South Korea. In this issue, we explore advancements being made in fuel cells, optoelectronics, stimuli-responsive materials, and nanofluidic membranes. Each of these areas is helping to advance multiple disciplines within the realm of materials science.

In our first article, Professor **Yung-Eun Sung (Seoul National University)** and colleagues examine fuel cells as one of the most promising energy conversion systems. They discuss some advancements in the area of polymer electrolyte membrane fuel cells (PEMFCs), to help get these more readily commercialized. They highlight platinum-group metal (PGM) catalysts and PMG-free to improve the oxygen reduction reaction (ORR) in PEMFCs. Additionally, they review some additional challenges in OOR catalyst development.

Professor **Byeong-soo Bae (Korea Advanced Institute of Science and Technology)** and colleagues discuss luminescent nanocrystals and their application in optical devices and color converting films, in our second article. They briefly introduce recent research about uniformly dispersed luminescent NC/siloxane composite resin synthesized via novel in-situ sol-gel condensation reaction in the presence of colloidal NC solution. They developed various siloxane-based wavelength converting composites which demonstrate high-performance and stability.

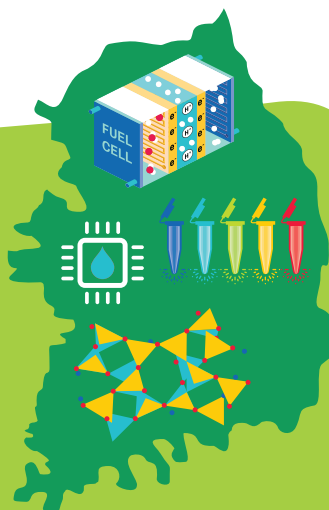
In our third article, Professor **Woo-Dong Jang (Yonsei University)** and colleagues review several poly(2-isopropyl-2-oxazoline)-based (P*i*PrOx) functional stimuli-responsive polymeric materials for application in the biomedical field, especially sensor applications. They review the preparation and modification of P*i*PrOx and discuss some of the exceptional properties of these materials.

And in our final article, Professor **Wooyoung Shim (Yonsei University)** and colleagues discuss natural clay materials for use as functional membranes. These materials are abundant with a nanosheet structure. They explore the structural arrangement and chemical properties of diverse phyllosilicate materials. They also discuss the application of these materials as nanofluidic membranes.

Each article in this publication concludes with a list of relevant SigmaAldrich materials available from Merck. For additional product information, please visit us at [SigmaAldrich.com/matsci](https://www.sigmaaldrich.com/matsci). If you have any new product suggestions, questions or comments, or new ideas for future *Material Matters*™ issues, please contact us at [SigmaAldrich.com/technicalservice](https://www.sigmaaldrich.com/technicalservice).

### About the Cover

Materials Science and Engineering Research is accelerating the progress of change in all aspects of our lives. Working together to solve real-world problems in nanotechnology, biotechnology, green energy, and many other research areas. This issue highlights some of the exciting research in South Korea, as such the cover displays the main themes of the issue overlaid onto the map of the country. Images of materials for use in fuel cells, displays, sensors, and membranes are displayed in the general region of the research institute. Our team is dedicated to advancing research around the world and we are excited to be able to highlight the contributions of some thought leaders from South Korea.



Merck KGaA  
Frankfurter Strasse 250  
64293 Darmstadt, Germany  
Phone +49 6151 72 0

#### To Place Orders / Customer Service

Contact your local office or visit  
[SigmaAldrich.com/order](https://www.sigmaaldrich.com/order)

#### Technical Service

Contact your local office or visit  
[SigmaAldrich.com/techinfo](https://www.sigmaaldrich.com/techinfo)

#### General Correspondence

Contact your local office or visit  
[SigmaAldrich.com/techinfo](https://www.sigmaaldrich.com/techinfo)

#### Subscriptions

Request your FREE subscription to *Material Matters*™ at [SigmaAldrich.com/mm](https://www.sigmaaldrich.com/mm)

The entire *Material Matters*™ archive is available at [SigmaAldrich.com/mm](https://www.sigmaaldrich.com/mm)

*Material Matters*™ (ISSN 1933-9631) is a publication of Merck KGaA and/or its affiliates

Copyright © 2022 Merck KGaA, Darmstadt, Germany and/or its affiliates. All rights reserved. Merck, the vibrant M, SigmaAldrich and Material Matters are trademarks of Merck KGaA, Darmstadt, Germany or its affiliates. All other trademarks are the property of their respective owners. Detailed information on trademarks is available via publicly accessible resources. More information on our branded products and services on [MerckMillipore.com](https://www.MerckMillipore.com)

# Table of Contents

## Articles

PGM and PGM-free Catalysts for Polymer Electrolyte Membrane Fuel Cells	3
Sol-Gel Derived Siloxane-Encapsulated Luminescent Nanocrystal Composites for Optoelectronics and Display	10
Poly(2-isopropyl-2-oxazoline)-based Multimodal Stimuli-responsive Functional Materials	22
Phyllosilicate Clay Minerals: Principles and Applications	30

## Featured Products

Fuel-Cell Membrane Materials A selection of Nafion, additives, and nanofibers	8
Exchange Membrane Materials A selection of proton, anion, and water exchange membranes	8
PDMS Materials A selection of terminated PDMS for optoelectronics	16
PDMS Copolymers and Other Siloxanes A selection PDMS copolymers and other siloxanes for optoelectronics	18
Silane Materials A selection of alkoxysilanes, silicon alkoxides, and silanes	19
Quantum Dot Materials A list of perovskite and CdS/ZnS QDs	20
Oxazolines A selection of low PDI, high $M_w$ , and functionalized poly(oxazoline)	27
Stimuli-Responsive Materials A selection of stimuli-responsive polymers	29
Phyllosilicate Materials A selection of nanoclays, polyacrylic acid materials, and other pyllsilicates	37

## Your Material Matters



Nicolynn Davis, Ph.D.  
Head of Material Sciences and F&F

Developed by Professor Mark Green at Kings College London, Conjugated Polymer Nanoparticles (CPNs) are highly fluorescent fluorophores that are brighter than the alternatives. They are available in 16 emission wavelengths compatible with the excitations of existing laser lines and filters. The portfolio covers the full visible spectrum through the near infrared (1000 nm) with various surface chemistries.

CPNs from Stream Bio boast several remarkable properties, such as high stability and photostability with no fading over time and an iron oxide core that makes them magnetic. Thanks to these properties, Stream Bio has demonstrated that CPNs are suitable for use in a wide range of applications, including microscopy, western blot, ELISA, stem cell tracking, and more.

Beyond these applications, CPNs have great potential in *in vitro* diagnostics, where their brightness can provide highly sensitive detection of many different protein targets. In lateral flow assays, CPNs have a 40% higher absorbance than conventional gold nanoparticles and research shows them to be approximately 100x more sensitive than europium chelates. Consequently, CPNs can enable highly sensitive detection, particularly for detecting low analyte levels. When incorporated into a Covid-19 antigen test, CPNs produced equivalent sensitivity to PCR, suggesting exciting future possibilities in the point-of-care IVD space.

CPNs are available through our e-commerce site, either as standalone or rapid conjugation kits (30 min and 60 min), which can be used for the conjugation of both antibodies and oligonucleotides. Visit [Sigma-Aldrich.com/CPN](https://www.sigmaaldrich.com/CPN) to review the complete list of products with fluorescence emissions ranging from 435 nm – 680 nm.

Name	Cat. No.
Conjugated Polymer Nanoparticle (CPN), fluorescence $\lambda_{em}$ 420 (violet), maleimide-thiol, 10 $\mu$ g antibody kit	4200MG5-1EA
Conjugated Polymer Nanoparticle (CPN), fluorescence $\lambda_{em}$ 1000 (IR-II), maleimide-thiol, 10 $\mu$ g antibody kit	1000MG5-1EA

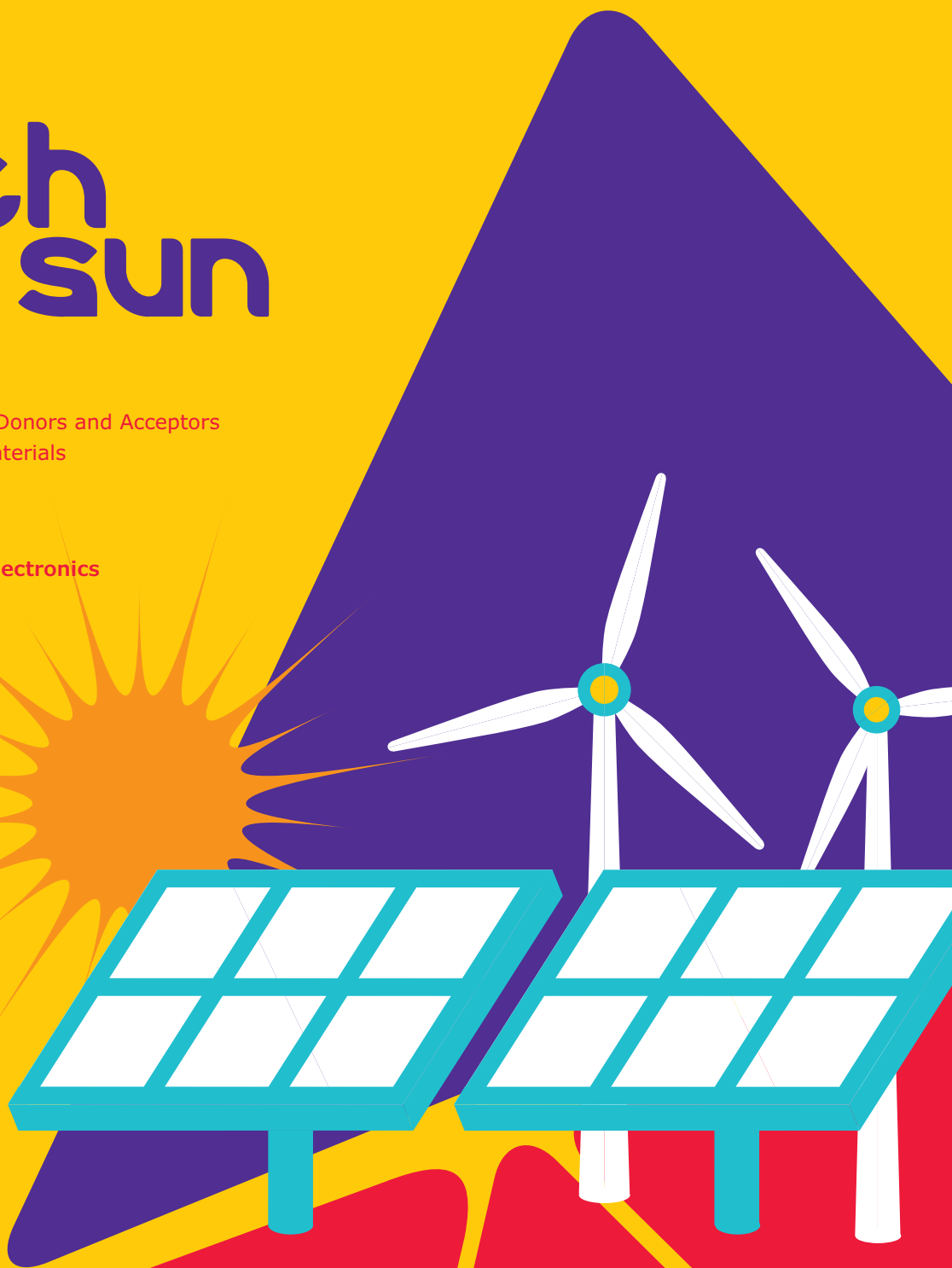
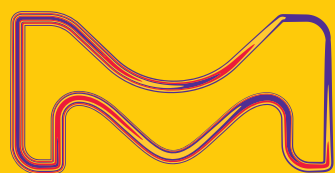
# catch the SUN

**Product Category list:**

- Organic Photovoltaic (OPV) Donors and Acceptors
- Dye-Sensitized Solar Cell Materials
- Perovskite Materials

Visit us at:

[SigmaAldrich.com/organic-electronics](https://SigmaAldrich.com/organic-electronics)



The life science  
business of Merck  
operates as  
MilliporeSigma in  
the U.S. and Canada.

**Sigma-Aldrich®**  
Lab & Production Materials

# PGM and PGM-free Catalysts for Polymer Electrolyte Membrane Fuel Cells



Sungjun Kim,<sup>1,2</sup> Min Her,<sup>1,2</sup> Yung-Eun Sung<sup>1,2\*</sup>

<sup>1</sup> Center for Nanoparticle Research, Institute for Basic Science (IBS), Seoul 08826, Republic of Korea

<sup>2</sup> School of Chemical and Biological Engineering, Seoul National University, Seoul 08826, Republic of Korea

\* Email: ysung@snu.ac.kr

## Introduction

Fuel cells generate energy efficiently through a carbon-neutral electrochemical process, making them one of the most promising energy conversion systems. Among the fuel cells, polymer electrolyte membrane fuel cells (PEMFCs) are the most mature technology and have significantly improved system performance and durability over the past decades. PEMFC applications such as fuel cell electric vehicles have become a reality with these advancements. However, PEMFC commercialization is still limited by high system costs owing to expensive components such as platinum-group metal (PGM) catalysts.<sup>1,2</sup> For example, in 2020, the estimated durability-adjusted cost (system cost to achieve 8,000 h of on-road operation) of 80 kW automotive PEMFC system with a production volume of 100,000 units per year was projected to be \$76/kW<sub>net</sub>, which was higher than the US Department of Energy (DOE) 2025 cost target of \$40/kW<sub>net</sub>.<sup>3</sup> In particular, the PEMFC cost breakdown identified that PGM catalysts accounted for nearly half the total cost of a stack in 80 kW PEMFC systems with a high-volume production scale. Therefore, to realize economically feasible PEMFCs, the primary task is to develop highly active and durable electrocatalysts, especially for the sluggish oxygen reduction reaction (ORR).

Along with a mechanistic understanding of ORR and advances in nanotechnology, there have been great strides in developing innovative ORR catalysts capable of reducing PGM loading while maintaining sufficient activity and stability. Currently, there are two catalyst development strategies. The first strategy is to significantly reduce PGM loading by maximizing PGM catalysts' activity and durability. The second is to develop a PGM-free catalyst that improves PEMFC performance. In this review, we highlight the recent progress in both PGM and PGM-free ORR catalysts for PEMFC applications. In addition, the remaining challenges in ORR catalyst development that meet the targets of PEMFC applications beyond the preliminary half-cell test are also discussed.

## PGM-based ORR Catalysts

The ORR is a complex electrochemical reaction involving various oxygenated intermediates. Pt-based nanoparticles have been commonly used to catalyze the ORR at the cathode. The ORR mechanism is not fully understood; however, fundamental studies using single-crystal surfaces have revealed that the intrinsic ORR activity strongly depends on the adsorption energy of the oxygenated intermediates on the active surface, following the Sabatier principle.<sup>4</sup> As shown in **Figure 1**, Pt is the most suitable single metal catalyst for the ORR. However, pure Pt binds the oxygenated species stronger than optimal; thus, the ORR activity is expected to be at the highest. Thus, the adsorption energy of the oxygenated intermediates on Pt must be weakened to increase the ORR activity. Alloying Pt with other transition metals can tune the electronic structure optimally. For example, incorporating early transition metals (Fe, Co, Ni, etc.) with a smaller atomic radius leads to compressive strain in the lattice, downshifting the Pt d-band center, resulting in a decrease in the oxygen binding energy of Pt. In addition, Pt-alloy catalysts with a core-shell structure, in which active Pt is selectively located on the outer shell over the cheaper transition metal core, enable high Pt utilization. The core transition metal present in the sub-surface below the Pt shell affects the electronic and geometric structure of Pt and can enhance the ORR activity of the Pt-enriched surface. After deliberate acid or heat treatment, a Pt-alloy catalyst can form a Pt-skin shell of an almost pure Pt layer. The resulting catalyst generally exhibits improved intrinsic ORR activity compared to the conventional core-shell type catalyst. Therefore, precise control of the near-surface composition of the Pt shell is essential for Pt-alloy catalysts.

The ORR kinetics on Pt and Pt-alloy surfaces are sensitive to the surface geometry and composition. For instance, the Pt<sub>3</sub>Ni(111) surface exhibited superior ORR activity compared to



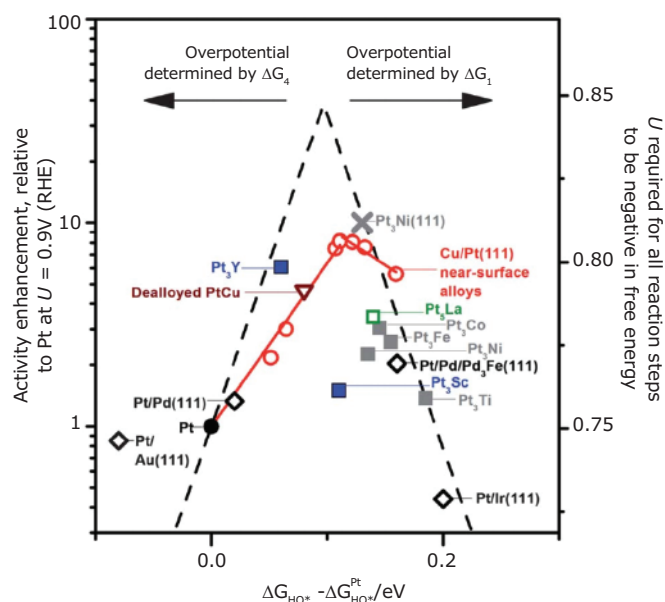


**Figure 1.** ORR activity plot as a function of the OH adsorption energy ( $\Delta G_{\text{HO}^*}$ ) for different catalysts with Pt-overlayers. Adapted with permission from reference 4, copyright 2012 Royal Society of Chemistry.

Pt<sub>3</sub>Ni(110) and Pt<sub>3</sub>Ni(100) facets in 0.1 M HClO<sub>4</sub> electrolyte.<sup>5</sup> The ORR kinetics sensitivity to surface facet structure has inspired the development of Pt-based polyhedral nanocrystals that can selectively expose specific crystal facets. The most representative example is the Pt-Ni bimetallic octahedra particles reported by Choi et al. Because the octahedral shape could maximize the highly active (111) crystal facets, the particles showed excellent specific activity (3.4 mA cm<sup>-2</sup>, 51-fold higher than that of Pt/C). Thus, they exhibited 17-fold higher mass activity (3.3 A mg<sub>Pt</sub><sup>-1</sup>) at 0.9 V over the Pt/C catalyst despite their low electrochemically active surface area (ECSA) of 31 m<sup>2</sup> g<sub>Pt</sub><sup>-1</sup>.<sup>6</sup> It is difficult to obtain polyhedral nanocrystals with a small particle size because such a metastable structure inevitably changes to a thermodynamically stable spherical shape. It is essential to maintain a highly active surface even in small particles to maximize the active sites at a given electrode for more efficient PGM material utilization. 3D hollow structures have been introduced because they can provide many active sites by exposing both the inner and outer surfaces for ORR while maintaining the highly functional crystal facets. Chen et al. reported a hollow Pt-Ni nano-frame catalyst prepared by selective leaching of transition metals from Pt-Ni polyhedral particles (Pt<sub>3</sub>Ni NFs in **Figure 2**).<sup>7</sup> The remaining frame not only had a high ECSA (67.2 m<sup>2</sup> g<sub>Pt</sub><sup>-1</sup>) but also well-exposed Pt<sub>3</sub>Ni(111) facets with superior ORR activity.

Consequently, the Pt-Ni nano-frame catalyst exhibited ORR mass activity of 5.7 A mg<sup>-1</sup> at 0.9 V. In addition to the 3D hollow nanostructure, other structurally modified catalysts have exhibited excellent ORR activity. Li et al. reported an ultrafine, jagged 1D Pt nanowire by dealloying Pt-Ni nanowire (J-Pt NWs in **Figure 2**).<sup>8</sup> The small radius nanowire (~ 2.2 nm) and rough

surface with jagged morphology showed high ECSA (118 m<sup>2</sup> g<sub>Pt</sub><sup>-1</sup>) and superior ORR mass activity of 13.6 A mg<sup>-1</sup> at 0.9 V.

Most of these delicately designed Pt-alloy catalysts show excellent initial ORR activity; however, the continuous leaching of the transition metal components during operation makes it difficult to maintain the desired surface composition and structure with superior ORR activity. Although the thermodynamically stable Pt-skin surface can mitigate the metal dissolution, more fundamental approaches to modifying the Pt-alloy system are required to improve the durability of ORR catalysts. Based on experimental and theoretical observations using well-controlled Au-Pt core-shell nanoparticles, our group found that inhibiting the formation of Pt oxide by maintaining a stable structure with low oxophilicity is critical to achieving high stability and ORR activity.<sup>9</sup> Thus, one promising approach is to incorporate a more stable third metal component into a bimetallic Pt-alloy system. Huang et al. demonstrated a significant improvement in the ORR activity and durability of Mo-doped Pt-Ni octahedral nanocrystals compared to their bimetallic counterparts (Mo-Pt<sub>3</sub>Ni in **Figure 2**).<sup>10</sup> Mo atoms preferentially located at the edges of the octahedral particle made the oxidation of Pt and Ni challenging during ORR, thereby inhibiting metal dissolution. An ordered intermetallic Pt-alloy system is another emerging strategy for alleviating the metal dissolution problem. Several seminal studies confirmed that the intermetallic phase is more stable than the disordered phase, and the intermetallic phase can suppress transition metal dissolution.<sup>1</sup> However, high-temperature annealing is usually required to obtain the ordered phase, which often causes the coalescence of nanoparticles during the process. To alleviate this problem, our group proposed the concept of carbon-shell encapsulating the nanoparticles.<sup>11</sup> By simply coating the disordered Pt-Fe nanoparticle with polydopamine during the annealing process, we obtained highly active, stable, ordered intermetallic Pt-Fe nanoparticles with a thin-layer N-doped carbon shell without any change in particle size. This ordered Pt-Fe catalyst exhibited higher activity and stability than the disordered Pt-Fe alloy and commercial Pt/C in a liquid half-cell condition. Moreover, the ordered Pt-Fe showed good long-term stability under practical operating conditions, showing only a 3.4 % decrease in performance after 100 h operation. During the same period, the performance of Pt/C decreased by 27%. This particular carbon encapsulating strategy is effective in terms of durability even with conventional Pt monometallic catalysts. For example, our group demonstrated that the PEMFC far exceeded the US DOE 2020 durability target using carbon-encapsulated Pt nanoparticles supported on a carbon nanofiber catalyst as the cathode.<sup>12</sup> While this strategy is effective in promoting durability, these intermetallic Pt-alloy catalysts do not show superior ORR activity compared to the catalysts mentioned earlier with unique nanostructures. Many intermetallic Pt-alloy catalysts have been successfully applied to single cells due to their high stability.<sup>13</sup> Recently, Chong et al. presented a new class of intermetallic Pt-alloy catalysts with a PGM-free catalytic substrate (LP@PF-2 in **Figure 2**).<sup>14</sup> The synergistic effect between the catalytic





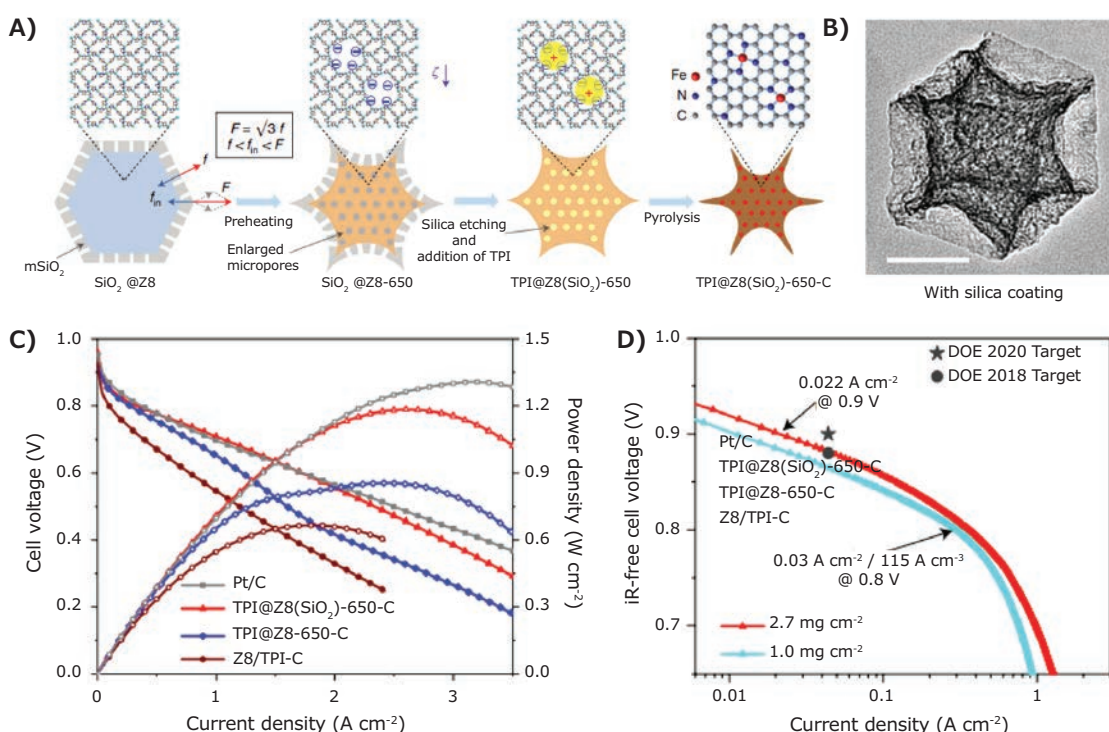


**Figure 3.** A) Schematic of the synthesis process and B) TEM image of ZIF-8-based Fe-N-C catalyst with a concave structure (TPI@Z8(SiO<sub>2</sub>)-650-C). C) Polarization and power density curves of the catalysts under 2.5 bar H<sub>2</sub>-O<sub>2</sub> and D) the Tafel plot used to determine mass activity of TPI@Z8(SiO<sub>2</sub>)-650-C under 1.0 bar H<sub>2</sub>-O<sub>2</sub>. Reproduced with permission from reference 19, copyright 2019 Nature Publishing Group.

Wan et al. reported a ZIF-8-derived Fe-N-C catalyst with a unique concave structure and high active site density (Figure 3).<sup>19</sup> Under the DOE testing protocol, the catalyst exhibited current densities of 47 mA cm<sup>-2</sup> at 0.88 V<sub>IR-free, cell</sub>, exceeding the 2018 DOE activity target for PGM-free catalyst (44 mA cm<sup>-2</sup> at 0.88 V<sub>IR-free, cell</sub>). They achieved high performance of 1.18 W cm<sup>-2</sup> under H<sub>2</sub>-O<sub>2</sub> (2.5 bar) conditions using the catalyst.

Despite the excellent performance of M-N-C catalysts, they still suffer from low durability, especially under oxidative and acidic environments at the cathode under practical operating conditions in PEMFCs.<sup>15</sup> Although the degradation mechanism of M-N-C catalysts is not fully understood; there is a consensus that the attack by oxidative species such as hydrogen peroxide on M-N<sub>x</sub> active sites or carbon matrix is one of the primary degradation mechanisms.<sup>20</sup> In Fe-N-C catalysts, oxidative free radicals generated by the Fenton-like reaction of dissolved Fe ions with hydrogen peroxide, a by-product of ORR, exacerbates this problem. Therefore, MOF-based catalysts using other transition metals such as Co and Mn instead of Fe have been developed to mitigate the attack by these radical species.

## Summary and Challenges

Recently, several innovative strategies have been proposed to achieve highly active and durable low-PGM or PGM-free ORR catalysts, and various Pt-alloy-based low-PGM catalysts and PGM-free catalysts with MOF-based carbon frameworks showed high activity and stability in preliminary half-cell tests in liquid

electrolytes. However, for practical fuel cell operation, the electrode requires a supply of gaseous oxygen to achieve high current operation, making the reactive interface more complex, requiring polymer (ionomers, such as Nafion) instead of liquid electrolytes. Thus, despite their promising activity and stability in half-cell conditions, most ORR catalysts still show inferior performance and durability in more complex and harsher single-cell conditions. This discrepancy in performance between half-cell and full-cell shows that the material must be designed with consideration for practical full-cell applications from the early stage of development of ORR catalysts. Therefore, it is necessary to better understand the physicochemical phenomena occurring at the catalyst-ionomer interfaces in a full-cell electrode beyond a liquid half-cell system.

## Author Contributions

The manuscript was written through the contributions of all the authors. All authors approved the final version of the manuscript.

## Notes

The authors declare that they have no known competing financial interests.

## Acknowledgment

This work was supported by the Institute for Basic Science (IBS-R006-A2).



## References

- (1) Wang, X. X.; Swihart, M. T.; Wu, G. *Nat. Catal.* **2019**, *2* (7), 578–589.
- (2) Chung, D. Y.; Yoo, J. M.; Sung, Y.-E. *Adv. Mater.* **2018**, *30* (42), 1704123.
- (3) Padgett, G. K. E. *US DOE Fuel Cell Technology Office* **2021**, Record # 21001.
- (4) Stephens, I. E. L.; Bondarenko, A. S.; Gronbjerg, U.; Rossmeisl, J.; Chorkendorff, I. *Energy Environ. Sci.* **2012**, *5* (5), 6744–6762.
- (5) Stamenkovic, V. R.; Fowler, B.; Mun, B. S.; Wang, G. F.; Ross, P. N.; Lucas, C. A.; Markovic, N. M. *Science* **2007**, *315* (5811), 493–497.
- (6) Choi, S. I.; Xie, S.; Shao, M.; Odell, J. H.; Lu, N.; Peng, H. C.; Protsailo, L.; Guerrero, S.; Park, J.; Xia, X.; Wang, J.; Kim, M. J.; Xia, Y. *Nano Lett.* **2013**, *13* (7), 3420–3425.
- (7) Chen, C.; Kang, Y. J.; Huo, Z. Y.; Zhu, Z. W.; Huang, W. Y.; Xin, H. L. L.; Snyder, J. D.; Li, D. G.; Herron, J. A.; Mavrikakis, M.; Chi, M. F.; More, K. L.; Li, Y. D.; Markovic, N. M.; Somorjai, G. A.; Yang, P. D.; Stamenkovic, V. R. *Science* **2014**, *343* (6177), 1339–1343.
- (8) Li, M. F.; Zhao, Z. P.; Cheng, T.; Fortunelli, A.; Chen, C. Y.; Yu, R.; Zhang, Q. H.; Gu, L.; Merinov, B. V.; Lin, Z. Y.; Zhu, E. B.; Yu, T.; Jia, Q. Y.; Guo, J. H.; Zhang, L.; Goddard, W. A.; Huang, Y.; Duan, X. F. *Science* **2016**, *354* (6318), 1414–1419.
- (9) Chung, D. Y.; Park, S.; Lee, H.; Kim, H.; Chung, Y.-H.; Yoo, J. M.; Ahn, D.; Yu, S.-H.; Lee, K.-S.; Ahmadi, M.; Ju, H.; Abruña, H. D.; Yoo, S. J.; Mun, B. S.; Sung, Y.-E. *ACS Energy Lett.* **2020**, 2827–2834.
- (10) Huang, X. Q.; Zhao, Z. P.; Cao, L.; Chen, Y.; Zhu, E. B.; Lin, Z. Y.; Li, M. F.; Yan, A. M.; Zettl, A.; Wang, Y. M.; Duan, X. F.; Mueller, T.; Huang, Y. *Science* **2015**, *348* (6240), 1230–1234.
- (11) Chung, D. Y.; Jun, S. W.; Yoon, G.; Kwon, S. G.; Shin, D. Y.; Seo, P.; Yoo, J. M.; Shin, H.; Chung, Y. H.; Kim, H.; Mun, B. S.; Lee, K. S.; Lee, N. S.; Yoo, S. J.; Lim, D. H.; Kang, K.; Sung, Y. E.; Hyeon, T. *J. Am. Chem. Soc.* **2015**, *137* (49), 15478–15485.
- (12) Karuppanan, M.; Kim, Y.; Gok, S.; Lee, E.; Hwang, J. Y.; Jang, J. H.; Cho, Y. H.; Lim, T.; Sung, Y. E.; Kwon, O. J. *Energy Environ. Sci.* **2019**, *12* (9), 2820–2829.
- (13) Fan, J.; Chen, M.; Zhao, Z.; Zhang, Z.; Ye, S.; Xu, S.; Wang, H.; Li, H. *Nat. Energy* **2021**, *6* (5), 475–486.
- (14) Chong, L.; Wen, J. G.; Kubal, J.; Sen, F. G.; Zou, J. X.; Greeley, J.; Chan, M.; Barkholtz, H.; Ding, W. J.; Liu, D. J. *Science* **2018**, *362* (6420), 1276.
- (15) Kim, J.; Yoo, J. M.; Lee, H. S.; Sung, Y. E.; Hyeon, T. *Trends Chem.* **2021**, *3* (9), 779–794.
- (16) Lefèvre, M. P., E.; Jaouen, F.; Dodelet, J.-P. *Science* **2009**, *324* (5923), 71–74.
- (17) Jung, E.; Shin, H.; Lee, B. H.; Efremov, V.; Lee, S.; Lee, H. S.; Kim, J.; Hooch Antink, W.; Park, S.; Lee, K. S.; Cho, S. P.; Yoo, J. S.; Sung, Y. E.; Hyeon, T. *Nat. Mater.* **2020**, *19* (4), 436.
- (18) Lee, S. H.; Kim, J.; Chung, D. Y.; Yoo, J. M.; Lee, H. S.; Kim, M. J.; Mun, B. S.; Kwon, S. G.; Sung, Y. E.; Hyeon, T. *J. Am. Chem. Soc.* **2019**, *141* (5), 2035–2045.
- (19) Wan, X.; Liu, X.; Li, Y.; Yu, R.; Zheng, L.; Yan, W.; Wang, H.; Xu, M.; Shui, J. *Nat. Catal.* **2019**, *2* (3), 259–268.
- (20) Choi, C. H.; Lim, H.-K.; Chung, M. W.; Chon, G.; Ranjbar Sahraie, N.; Altin, A.; Sougrati, M.-T.; Stievano, L.; Oh, H. S.; Park, E. S.; Luo, F.; Strasser, P.; Dražić, G.; Mayrhofer, K. J. J.; Kim, H.; Jaouen, F. *Energy Environ. Sci.* **2018**, *11* (11), 3176–3182.

## Nafion™

Name	Greener Alternative Category	Description	Solubility / Concentration	Cat. No.
Nafion™ perfluorinated membrane	enabling	8 in. × 10 in.	H <sub>2</sub> O: insoluble	274674-1EA
Nafion™ perfluorinated resin solution	enabling	0.924 g/mL at 25 °C	5 wt. % in mixture of lower aliphatic alcohols and water	527084-25ML
	enabling	1.02 g/mL at 25 °C	20 wt. % in lower aliphatic alcohols and water	663492-25ML 663492-100ML
	enabling	1.01-1.03 g/cm <sup>3</sup> at 25 °C	20 wt. % in mixture of lower aliphatic alcohols and water	527122-25ML 527122-100ML
Perfluorinated membrane made from Nafion™ 117	enabling	12 in. × 12 in. × 0.007 in.	-	292567-1EA
Perfluorinated resin solution containing Nafion™ 1100W	enabling	0.874 g/mL at 25 °C	5 wt.% in lower aliphatic alcohols and water	274704-25ML 274704-100ML 274704-500ML

## Additives

Name	Particle Size	Description	Form	Cat. No.
Polysulfone	-	average Mn ~16,000 by MO average Mw ~35,000 by LS	pellets (transparent)	428302-100G 428302-500G
	-	average Mn ~22,000 by MO	beads pellets	182443-5G 182443-250G
Poly(tetrafluoroethylene)	1 μm	density: 2.15 g/mL at 25 °C	powder (free-flowing)	430935-5G 430935-100G
	≤12 μm	density: 2.15 g/mL at 25 °C	powder (free-flowing)	430943-5G 430943-100G
	35 μm	density: 2.1 g/mL at 25 °C	powder	468096-5G 468096-100G
	>40 μm	density: 2 g/mL at 25 °C	powder	182478-100G 182478-250G
Titanium(IV) oxide	<100 nm (BET)	-	nanopowder	677469-5G
	21 nm (TEM)	-	nanopowder	718467-100G
Tungsten(IV) carbide	2 μm	-	powder	241881-100G

## Nanofibers

Name	Fiber Size (diam. x L)	Primary Crystallite Size	Crystal Phase	Cat. No.
Aluminum oxide milled nanofibers alpha alumina	300-900 nm x 2-10 μm	-	alpha	914681-10G 914681-5G
Aluminum oxide nanofibers	monoclinic and tetragonal	7 nm	gamma	913499-5G 913499-10G
Cerium Zirconium oxide nanofiber (Ce:Zr ratio 50:50)	300-800 nm x 2-hundreds of μm	8 nm	tetragonal	912239-5G 912239-10G
Cerium Zirconium Oxide Milled Nanofiber (Ce:Zr ratio 50:50)	300-800 nm x 210 μm	8 nm	tetragonal	914940-5G 914940-10G
Silica dioxide sorbent milled nanofiber	300-800 nm	-	-	914150-5G 914150-10G
Silica dioxide-electrospun milled nanofibers	100-300 nm x 2-10 μm	-	-	913944-10G 913944-5G
Silica dioxide sorbent nanofiber	800-1200 nm	-	-	912492-5G 912492-10G
Silica dioxide vitreous milled nanofiber	-	-	-	914657-5G 914657-10G
Titanium dioxide nanofibers	200-800 nm x 2-hundreds of μm	-	anatase	913480-10G 913480-5G
Titanium dioxide milled nanofibers	200-800 nm x 2-10 μm	10 nm	anatase-rutil	914401-10G 914401-5G
Zirconium oxide milled nanofibers	200-800 nm x 2-10 μm	8-13 nm	monoclinic and tetragonal	913685-5G 913685-10G
Zirconium oxide nanofibers	200-800 nm x 2-hundreds of μm	8-13 nm	monoclinic and tetragonal	913510-5G 913510-10G

## Fuel-Cell Membranes

### Proton-Exchange Membranes

Name	L x W (cm)	Thickness (μm)	Cat. No.	Name	L x W (cm)	Thickness (μm)	Cat. No.
Xion PEM-Aquivion®-720	5 x 5	5	PEM3A0522-1EA	Xion PEM-Dyneon-725	5 x 5	5	PEM1A0522-1EA
	5 x 5	10	PEM3A1022-1EA		5 x 5	10	PEM1A1022-1EA
	5 x 5	20	PEM3A2022-1EA		5 x 5	20	PEM1A2022-1EA
	5 x 5	30	PEM3A3022-1EA		5 x 5	30	PEM1A3022-1EA
	5 x 5	50	PEM3A5022-1EA		5 x 5	50	PEM1A5022-1EA
	10 x 10	5	PEM3A0544-1EA		10 x 10	5	PEM1A0544-1EA
	10 x 10	10	PEM3A1044-1EA		10 x 10	10	PEM1A1044-1EA
	10 x 10	20	PEM3A2044-1EA		10 x 10	20	PEM1A2044-1EA
	10 x 10	30	PEM3A3044-1EA		10 x 10	30	PEM1A3044-1EA
	10 x 10	50	PEM3A5044-1EA		10 x 10	50	PEM1A5044-1EA
	15 x 15	5	PEM3A0566-1EA		15 x 15	5	PEM1A0566-1EA
	15 x 15	10	PEM3A1066-1EA		15 x 15	10	PEM1A1066-1EA
	15 x 15	20	PEM3A2066-1EA		15 x 15	20	PEM1A2066-1EA
	15 x 15	30	PEM3A3066-1EA		15 x 15	30	PEM1A3066-1EA
	15 x 15	50	PEM3A5066-1EA		15 x 15	50	PEM1A5066-1EA
Xion PEM-Aquivion®-830	5 x 5	5	PEM3B0522-1EA	Xion PEM-Dyneon-800	5 x 5	5	PEM1B0522-1EA
	5 x 5	10	PEM3B1022-1EA		5 x 5	10	PEM1B1022-1EA
	5 x 5	20	PEM3B2022-1EA		5 x 5	20	PEM1B2022-1EA
	5 x 5	30	PEM3B3022-1EA		5 x 5	30	PEM1B3022-1EA
	5 x 5	50	PEM3B5022-1EA		5 x 5	50	PEM1B5022-1EA
	10 x 10	5	PEM3B0544-1EA		10 x 10	5	PEM1B0544-1EA
	10 x 10	10	PEM3B1044-1EA		10 x 10	10	PEM1B1044-1EA
	10 x 10	20	PEM3B2044-1EA		10 x 10	20	PEM1B2044-1EA
	10 x 10	30	PEM3B3044-1EA		10 x 10	30	PEM1B3044-1EA
	10 x 10	50	PEM3B5044-1EA		10 x 10	50	PEM1B5044-1EA
	15 x 15	5	PEM3B0566-1EA		15 x 15	5	PEM1B0566-1EA
	15 x 15	10	PEM3B1066-1EA		15 x 15	10	PEM1B1066-1EA
	15 x 15	20	PEM3B2066-1EA		15 x 15	20	PEM1B2066-1EA
	15 x 15	30	PEM3B3066-1EA		15 x 15	30	PEM1B3066-1EA
	15 x 15	50	PEM3B5066-1EA		15 x 15	50	PEM1B5066-1EA

Name	L x W (cm)	Thickness (µm)	Cat. No.
Xion PEM-Nafion™-1000	5 x 5	5	PEM2A0522-1EA
	5 x 5	10	PEM2A1022-1EA
	5 x 5	20	PEM2A2022-1EA
	5 x 5	30	PEM2A3022-1EA
	5 x 5	50	PEM2A5022-1EA
	10 x 10	5	PEM2A0544-1EA
	10 x 10	10	PEM2A1044-1EA
	10 x 10	20	PEM2A2044-1EA
	10 x 10	30	PEM2A3044-1EA
	10 x 10	50	PEM2A5044-1EA
	15 x 15	5	PEM2A0566-1EA
	15 x 15	10	PEM2A1066-1EA
	15 x 15	20	PEM2A2066-1EA
	15 x 15	30	PEM2A3066-1EA
	15 x 15	50	PEM2A5066-1EA
Xion PEM-Nafion™-1100	5 x 5	5	PEM2B0522-1EA
	5 x 5	10	PEM2B1022-1EA
	5 x 5	20	PEM2B2022-1EA
	5 x 5	30	PEM2B3022-1EA
	5 x 5	50	PEM2B5022-1EA
	10 x 10	5	PEM2B0544-1EA
	10 x 10	10	PEM2B1044-1EA
	10 x 10	20	PEM2B2044-1EA
	10 x 10	30	PEM2B3044-1EA
	10 x 10	50	PEM2B5044-1EA
	15 x 15	5	PEM2B0566-1EA
	15 x 15	10	PEM2B1066-1EA
	15 x 15	20	PEM2B2066-1EA
	15 x 15	30	PEM2B3066-1EA
	15 x 15	50	PEM2B5066-1EA

## Anion-Exchange Membranes

Name	L x W (cm)	Thickness (µm)	Cat. No.
Xion AEM-Pention-72-5CL	5 x 5	5	AEM2A0522-1EA
	5 x 5	10	AEM2A1022-1EA
	5 x 5	20	AEM2A2022-1EA
	5 x 5	30	AEM2A3022-1EA
	5 x 5	50	AEM2A5022-1EA
	10 x 10	5	AEM2A0544-1EA
	10 x 10	10	AEM2A1044-1EA
	10 x 10	20	AEM2A2044-1EA
	10 x 10	30	AEM2A3044-1EA
	10 x 10	50	AEM2A5044-1EA
	15 x 15	5	AEM2A0566-1EA
	15 x 15	10	AEM2A1066-1EA
	15 x 15	20	AEM2A2066-1EA
	15 x 15	30	AEM2A3066-1EA
	15 x 15	50	AEM2A5066-1EA

Name	L x W (cm)	Thickness (µm)	Cat. No.
Xion AEM-Pention-72-15CL	5 x 5	5	AEM2B0522-1EA
	5 x 5	10	AEM2B1022-1EA
	5 x 5	20	AEM2B2022-1EA
	5 x 5	30	AEM2B3022-1EA
	5 x 5	50	AEM2B5022-1EA
	10 x 10	5	AEM2B0544-1EA
	10 x 10	10	AEM2B1044-1EA
	10 x 10	20	AEM2B2044-1EA
	10 x 10	30	AEM2B3044-1EA
	10 x 10	50	AEM2B5044-1EA
	15 x 15	5	AEM2B0566-1EA
	15 x 15	10	AEM2B1066-1EA
	15 x 15	20	AEM2B2066-1EA
	15 x 15	30	AEM2B3066-1EA
	15 x 15	50	AEM2B5066-1EA
Xion AEM-Durion II-LMW	5 x 5	5	AEM1A0522-1EA
	5 x 5	10	AEM1A1022-1EA
	5 x 5	20	AEM1A2022-1EA
	5 x 5	30	AEM1A3022-1EA
	10 x 10	5	AEM1A0544-1EA
	10 x 10	10	AEM1A1044-1EA
	10 x 10	20	AEM1A2044-1EA
	10 x 10	30	AEM1A3044-1EA
	15 x 15	5	AEM1A0566-1EA
	15 x 15	10	AEM1A1066-1EA
	15 x 15	20	AEM1A2066-1EA
	15 x 15	30	AEM1A3066-1EA

## Water-Exchange Membranes

Name	L x W (cm)	Thickness (µm)	Cat. No.
Xion WEM-Hydrax-200	5 x 5	30	WEM1A3022-1EA
	5 x 5	50	WEM1A5022-1EA
	10 x 10	30	WEM1A3044-1EA
	10 x 10	50	WEM1A5044-1EA
	15 x 15	30	WEM1A3066-1EA
	15 x 15	50	WEM1A5066-1EA

# Sol-Gel Derived Siloxane-Encapsulated Luminescent Nanocrystal Composites for Optoelectronics and Display



Junho Jang, Yongmin Shin, Seungwan Kim, and Byeong-Soo Bae\*

Wearable Platform Materials Technology Center (WMC), Laboratory of Optical Materials and Coatings (LOMC), Department of Materials Science and Engineering, Korea Advanced Institute of Science and Technology (KAIST), Daehak-ro 294, Yuseong-gu, Daejeon 34141, Republic of Korea  
\*Email: bsbae@kaist.ac.kr

## Introduction

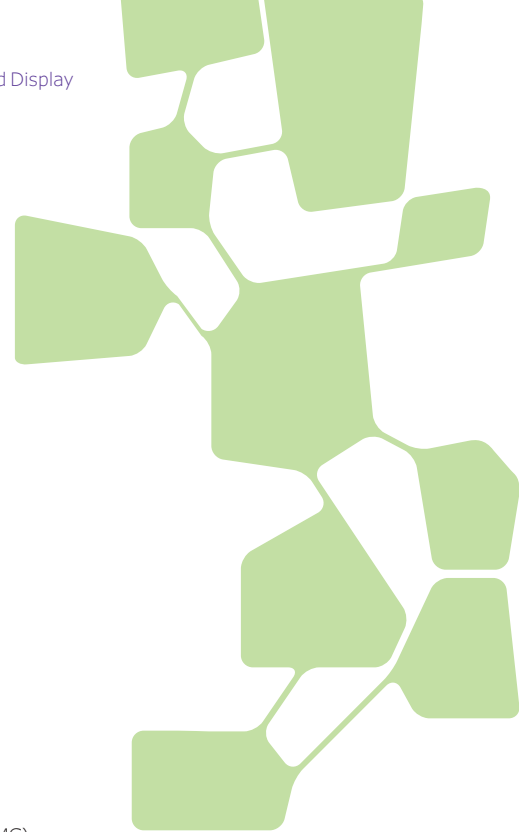
Luminescent nanocrystals (NCs), including lanthanide-doped nanocrystals (upconversion nanoparticles, UCNPs), semiconducting nanocrystals (quantum dots, QDs), and metal halide perovskite NCs (PNCs), show promise as high-performance wavelength converting materials. These materials have unique optical properties like a large Stoke or anti-Stoke shift, narrow emission spectra, and color tunability depending on size and compositional changes, allowing the up- or down-converting of luminescence for various applications in optical multiplexing devices, optoelectronics, and displays.<sup>1,2</sup> However, the photoluminescence (PL) of NCs is significantly decreased by exposure to high temperature, high humidity, and chemicals due to their high vulnerability to oxygen and moisture.<sup>3-5</sup> Core/shell (including multi-shell, alloyed shell, or giant shell) structures passivated by various organic ligands have been widely studied to prevent decay of optical properties however, they still show insufficient stability.<sup>1,6,7</sup>

Dispersing NCs in an optical-grade polymeric resin can result in variable functionality, making it a practical layer in wavelength-converting applications.<sup>7-10</sup> Most NC-dispersed polymer composites are fabricated by physically blending the NCs with a polymer matrix, which can cause aggregation and/or phase separation of the NCs due to compatibility issues, resulting in optical property degradation from external environments.<sup>9,11</sup> Various methods have been suggested to overcome these challenges, such as forming an inorganic layer on the NC surface using a ligand-exchange process.<sup>8,9,12</sup> These strategies still show limited NC stability under elevated temperature with high humidity and require complex processing or additional protecting

layers to ensure uniformity and stability.<sup>13</sup> Highly stable, uniformly dispersed NC composites and no protecting processes are desirable for use in practical applications.

Sol-gel derived siloxane hybrid materials, fabricated by polymerization of siloxane resins synthesized by sol-gel reaction of organo-silane precursors, have been widely utilized due to their hybridized properties of both organic and inorganic characteristics, including optical transparency, flexibility, mechanical strength, and thermal stability.<sup>14</sup> In particular, the siloxane hybrid material functionality can be easily modified by controlling organic groups of silane precursors and the molecular structure of siloxane networks via sol-gel reaction methods, thereby providing effective encapsulation of various molecules and nanomaterials.<sup>9,10,13</sup>

In this review, we briefly introduce recent research about a stable and uniformly dispersed luminescent NC/siloxane composite resin synthesized via a novel in-situ sol-gel condensation reaction of silane precursors in the presence of colloidal NC solution.<sup>8-10,13</sup> In-situ sol-gel process means that NCs passivated by organic ligands are chemically dispersed at the initial synthesis stage of the siloxane resin. By chemically encapsulating the NCs in the siloxane matrix at the molecular scale, we achieved greatly improved stability of the NCs in various harsh environments of high temperature with high humidity and chemicals without ligand-exchange processes and additional protecting layers. We developed various types of siloxane-based wavelength converting composites using UCNPs, inorganic Cd-based QDs, and PNCs demonstrating high-performance, stable optical devices and color converting films.



## Near Infrared to Visible Converting Siloxane-Encapsulated UCNP Hybrid

UCNPs that emit visible light under near-infrared (NIR) irradiation have been applied in multimodal imaging, cancer therapy, luminescent solar concentrators, and displays due to their unique opto-physical properties such as large anti-Stokes shift, sharp emission bands, and low autofluorescence.<sup>5,10</sup> For the synergistic effect of functionality and application, UCNPs are easily integrated with various transparent polymers by simple blending, one of the most popular techniques for fabrication of composites, which makes hybridized characteristics of both the inorganic UCNPs (multi-photon absorption and anti-Stokes shift) and the organic polymers (flexibility, processibility, and functionality).<sup>5</sup> Following the integration of UCNPs and transparent polymers, they find applications in various fields such as display, optoelectronics, sensors, actuators, patterning, and encoding.<sup>5</sup>

Although they have various advantages, the luminescent efficiency of UCNPs can be degraded by the quenching effect originating from a non-radiative relaxation in the energy level of surface defects or impurities caused by the rise in temperature, the existence of water molecules, and chemical damage from pH changes.<sup>10,15</sup> These instabilities hinder the operation of UCNP-based composites under actual environmental conditions. Core/shell structures with ligand-exchange to various organic functional groups have been tried, but these still exhibited limited stability, and degradation of luminescent efficiency during ligand-exchange processes.<sup>10,15</sup>

By considering these issues, a siloxane-encapsulated UCNP (SE-UCNP) composite with stable PL performance has been developed using novel in-situ sol-gel processes. Green ( $\text{NaYF}_4:\text{Yb}$ , Er) and blue ( $\text{NaYF}_4:\text{Yb}$ , Tm) emitting UCNPs passivated by oleic acid (OA) were dispersed during sol-gel condensation reaction of silane precursors containing 3-methacryloxypropyltrimethoxysilane (MPTS, Cat. No. 440159) and diphenylsilanediol (DPSD, Cat. No. D213705), forming viscous and luminescent UCNP-oligosiloxane

resin. Then, SE-UCNP was solidified via a UV-induced curing process (Figure 1A).<sup>10</sup> During the fabrication process of SE-UCNP, retaining optical properties of UCNPs (Figure 1B) and chemical crosslinking between OA (from UCNPs) and methacrylate groups (from siloxane matrix) (Figure 1C) with uniform distribution (Figure 1D) were confirmed.

We investigated the PL stability of the SE-UCNPs under high temperature and humidity (i.e., 85 °C/85% relative humidity (RH)) and various pH conditions. Our SE-UCNPs retained their initial PL intensity for 40 days, at 85 °C/85% RH even when exposed to a high humidity environment that causes luminescence degradation of UCNPs (Figure 2A). In addition, we found that the SE-UCNPs exhibited unchanged PL intensity over a broad range of pH (from 1 to 14), indicating excellent chemical stability (Figure 2B). As a demonstration of SE-UCNPs for practical application, the fabrication of a two-color binary micro-barcode printed on various flexible or biological substrates (money, credit card, and human hand) exhibited easy detection under NIR ( $\lambda = 980 \text{ nm}$ ) laser excitation using an optical microscope or a mobile phone camera (Figure 2C).

## Highly Stable Siloxane-Encapsulated QD Hybrid for Color Converter in Displays

QDs show promise as color converting materials for next-generation display applications due to their unique optical properties such as size-dependent color tunability, high color purity, wide color range, and high PL quantum yield (PLQY). However, QD vulnerability to oxygen and moisture causes significant degradation of the PL performance during device fabrication and long-term operations, hindering practical applications.<sup>6</sup> Currently, a color converting QD film in a liquid crystal display (LCD) backlight unit (BLU) using blue LEDs was developed for use in displays, where QDs were physically blended in optical grade polymeric matrixes and sandwiched between two barrier films to prevent the diffusion of oxygen and moisture.<sup>9</sup> Although dispersion and stability of QDs in

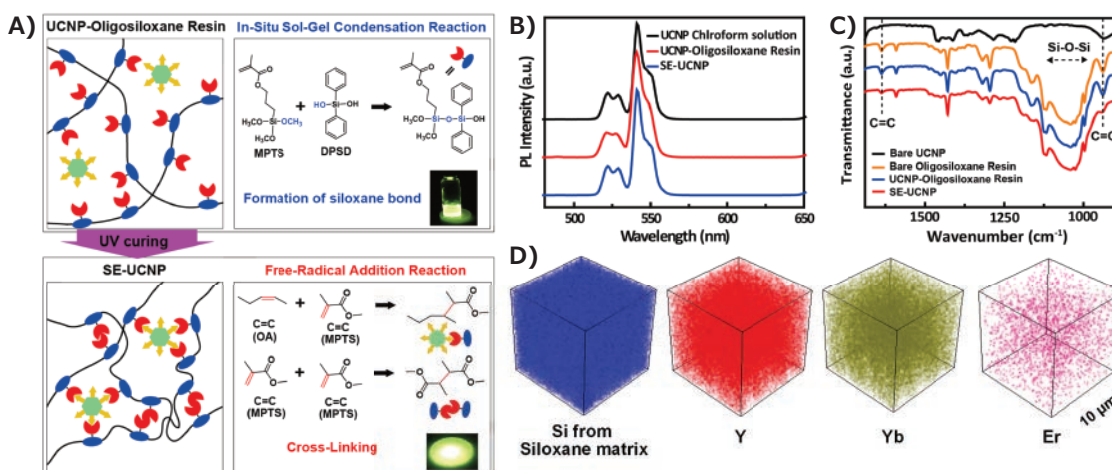


**Figure 1.** A) Schematic illustration of fabricating SE-UCNP. B) Change of PL spectra during the fabrication process of SE-UCNP. C) Change of FT-IR spectra during fabrications of SE-UCNP. D) TOF-SIMS 3D images of the SE-UCNP: Si, Y, Yb, and Er ( $1000 \mu\text{m}^3$  of the cube). Reprinted with permission from reference 11, copyright 2017 Wiley.



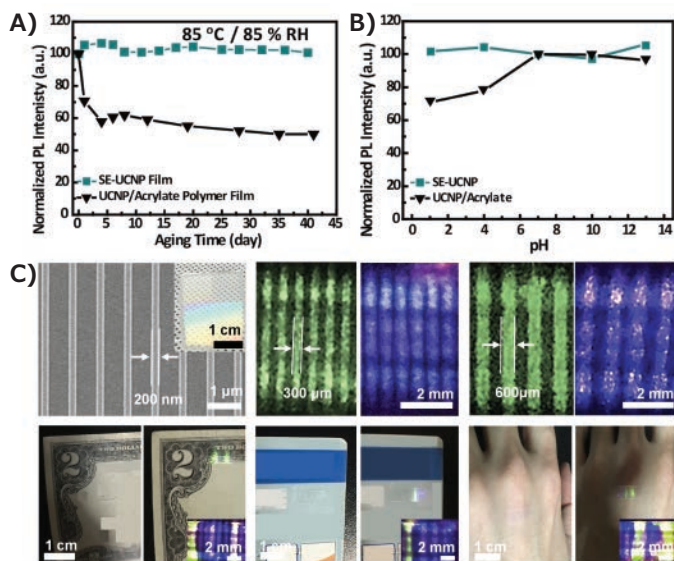


**Figure 2.** A) Change of PL emission intensity of SE-UCNP after 40 days at 85 °C/85% RH (980 nm NIR irradiation). B) PL intensity change of SE-UCNP according to different pH conditions. C) Photographs of fabricated micro-barcodes on substrates such as E) currency, F) a credit card, and G) human skin. Insets are images of the micro-barcodes acquired by the mobile phone camera. Reprinted with permission from reference 11, copyright 2017 Wiley.

a conventional optical resin have been attempted via the ligand-exchange process, several limitations remained such as inevitably decreased PLQY of QDs during the ligand-exchange processes, still low uniformity and stability, necessity of additional protecting layers for long-term stability under high temperature and humidity, which are huge obstacles to their commercialization.<sup>6</sup> Therefore, uniformly distributed, stable QDs containing polymer resin should be developed.

Based on these considerations, we have developed a siloxane-encapsulated QD hybrid through an in-situ sol-gel condensation reaction of various silane precursors. They are for highly stable color converting layers or films in which QDs consist of Cd-based core/Zn-based shell structure and are passivated by OA. Early development work in our group focused on the synthesis of UV-curable QD/siloxane resins to fabricate stable PL films without additional barrier layers and ligand-exchange processes for application in on-surface type that apply to film state on BLU. Similar to the fabrication of SE-UCNPs, colloidal QDs were chemically dispersed in a siloxane matrix at the initial stage of resin synthesis.<sup>9</sup> Following UV-curing, a QD/siloxane hybrid composite film with chemical crosslinking between OA of QDs and methacrylate of the siloxane matrix was obtained (Figure 3A). During fabrication, the optical properties of the QDs were maintained (Figure 3B), excellent dispersion stability for long-term storage (Figure 3C), and uniform emission characteristics (Figure 3D) with a homogeneous distribution of QDs in the siloxane matrix (Figure 3E) were confirmed. We investigated thermal stability of QD/siloxane hybrid confirmed by tracing PLQY under high temperature conditions (85 °C/5% RH), which exhibited unchanged PLQY during 40 days aging (Figure 3F).

Interestingly, the PLQY of a QD/siloxane hybrid aged at high temperature and high humidity (85 °C/85% RH) is noticeably increased in the first 2 days and retained its value for an additional 40 days after (Figure 3G). This was due to water adsorption on the surface of QDs in the siloxane matrix that induces passivation of surface defects in QDs.<sup>9</sup> By combining these results, we confirmed excellent thermal stability of the QD/siloxane hybrid when chemical crosslinking between surface ligands of QDs and a siloxane matrix occurs.

While the UV-curable QD/siloxane hybrid (PSE-QD) exhibited excellent thermal stability, it is more desirable for applying on-chip type structure that directly encapsulated the QDs in the LED packaging. For this, PSE-QDs have several limitations, such as incomplete curing due to UV absorption of the QDs, low thermal degradation temperature of methacrylate groups, the necessity to use thermal curing, and high refractive index of the resin for LED encapsulation.<sup>8</sup> Thus, reliable QD-containing LED encapsulation materials that contain uniformly distributed QDs in a thermally stable optical resin with a high refractive index are necessary.

Following these studies, we developed QD-dispersed encapsulating materials (TSE-QD) using a thermally curable and stable siloxane hybrid matrix via an in-situ sol-gel process. QD-dispersed siloxane resin (QD/siloxane resin) was synthesized using diethoxymethylsilane (DEMS) and DPSD in the presence of QDs. For thermal-curing, a crosslinker was also synthesized by using a non-hydrolytic sol-gel condensation reaction between dimethoxymethylvinylsilane (Cat. No. 446203) and DPSD. The thermal-induced hydrosilylation reaction induced formation of the QD-contained siloxane composite (TSE-QD) (Figure 4A). The optical properties of QDs (Figure 4B) did not degrade, keeping uniform distribution in the siloxane matrix (Figure 4C) even during the high-temperature processes. Additionally, the siloxane matrix of TSE-QDs has a high refractive index (> 1.57) due to the high phenyl content in the siloxane matrix.<sup>16</sup>

By using a robust siloxane matrix, we can achieve exceptionally high thermal stability of TSE-QDs in which the PLQY of TSE-QDs exhibited much less degradation compared to PSE-QDs and QDs with conventional acrylate-based composites under extremely high temperatures (120 °C in ambient air, Figure 4D). TSE-QDs also showed greatly improved chemical stability compared to other reference samples in alcohol, which can easily detach the surface ligands of QDs. Therefore, we developed a QD-contained LED encapsulating material with excellent thermal and chemical stability with uniform dispersion via in-situ sol-gel process and thermal curing method.

To demonstrate a practical application, we fabricated white LEDs which are directly encapsulated by yellow-emitting TSE-QDs that combine red- and green-emitting QDs in a siloxane matrix; the resulting devices showed natural white light and a wide color gamut (116% of the national television systems committee (NTSC) 1931), where the color coordinates of the red TSE-QDs

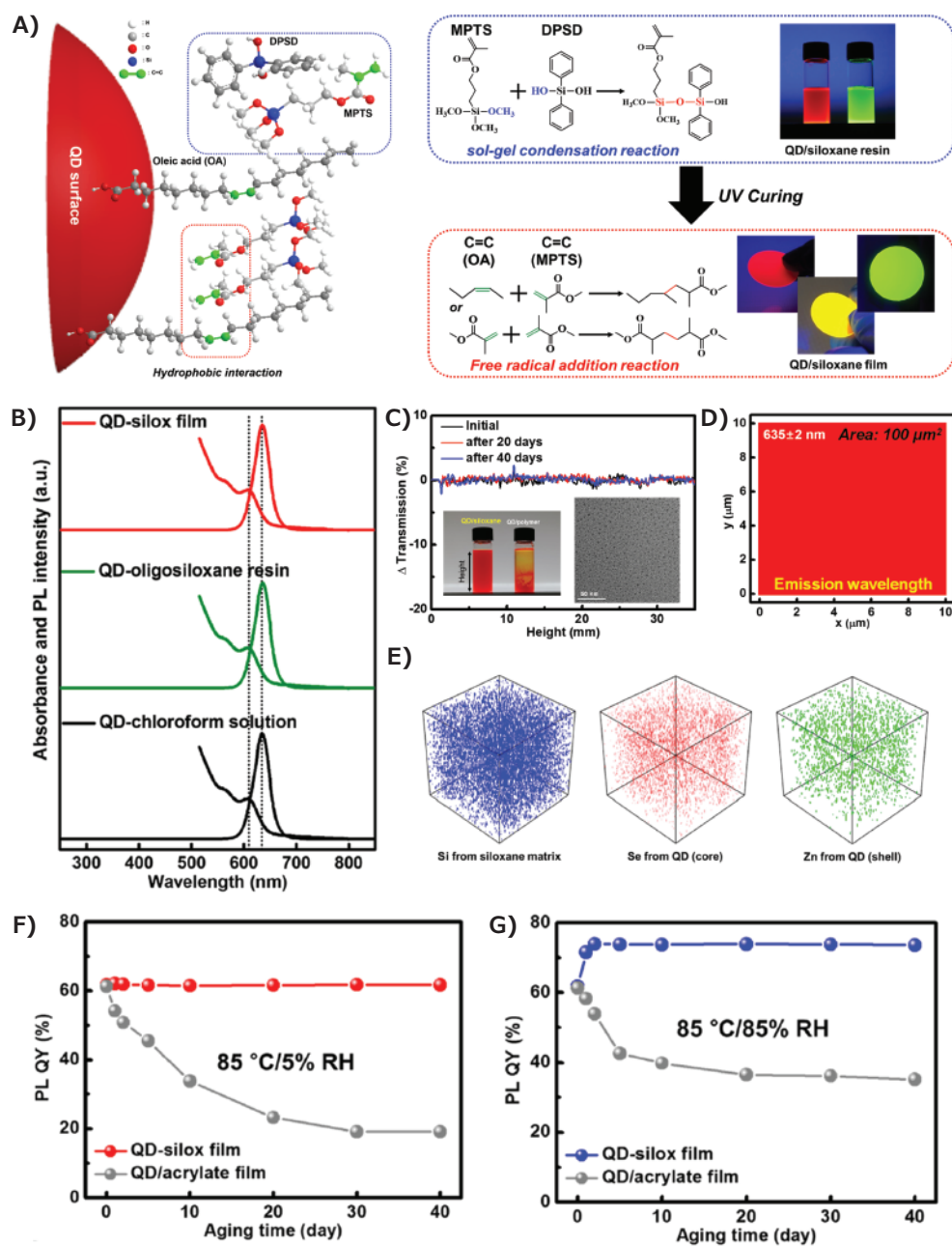


**Figure 3.** A) Fabrication process of QD/siloxane hybrid. B) Change of PL spectrum during fabrications. (C-E) Results of uniformity confirming C) Delta transmission spectra, D) RAMAN-PL analysis, and E) TOF-SIMS 3D images. (F-G) Traces of PLQY of QD/siloxane hybrid during testing at F) 85 °C/5% RH and G) 85 °C/85% RH. Reprinted with permission from reference 10, copyright 2019 American Chemical Society.

(0.702, 0.287), green TSE-QDs (0.265, 0.715), blue LEDs (0.153, 0.023), and white LEDs (0.315, 0.323) occur in the Commission Internationale De l'Eclairage (CIE) color space (Figure 5A). The fabricated white LED exhibited a monotonic increase when the forward bias current increased from 10 to 100 mA (Figure 5B) and unchanged PL intensity in 85 °C with 85% RH (Figure 5C), which indicates excellent photostability and reliability. Based on these results, we find that our TSE-QDs are a promising candidate for use as luminescent LED encapsulation materials for on-chip type structures.

Several issues impede the development of QD-based color filters using conventional photoresist (PR) materials or monomers; color filters must possess patternability and remain stable under light irradiation and external environments. We developed stable QD-siloxane based PRs via surface modification of QDs and a thiol-ene derived photo-curing reaction.<sup>17</sup> Moreover, we are currently developing a QD-siloxane-based ink with low viscosity and high stability. By using them, we will demonstrate full color micro-LED that will be published soon in our group.

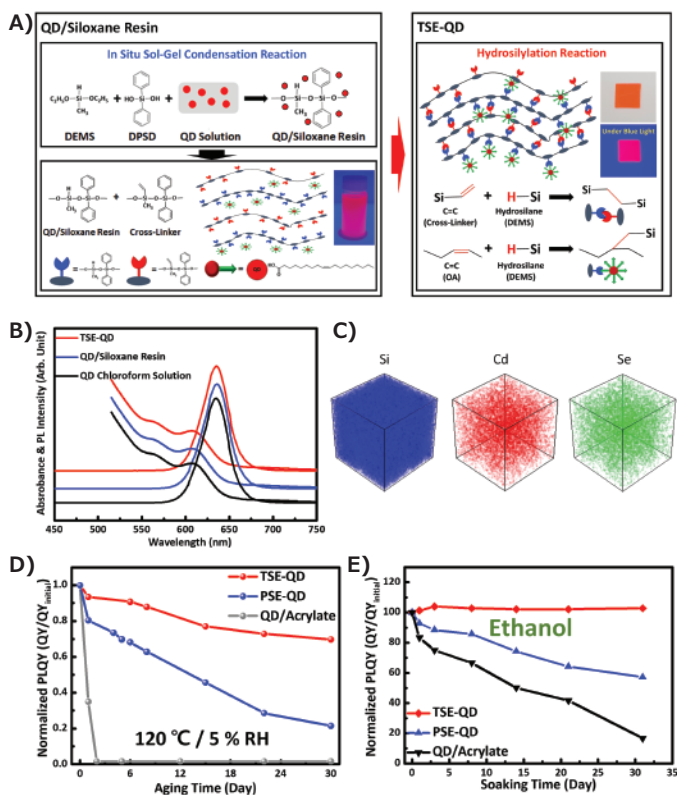


**Figure 4.** A) Schematic illustration of the fabrication of TSE-QD. B) Change of PL spectra during the thermal curing process. C) TOF-SIMS 3D images after the thermal curing process. (D-E) Stability of TSE-QD under D) high temperature and E) alcohol. Reprinted with permission from reference 9, copyright 2016 American Chemical Society.

## Chemically Encapsulated PNC by Siloxane Matrix for High-performance and Stable Color Converting Layer in Displays

Metal halide perovskites with  $ABX_3$  structure (A: organic cation, B: metal cation, X: halogen anion) have emerged as a new class of material for various optoelectronic applications. The power conversion efficiency of perovskite-based solar cells has been rapidly increased to over 25.2%.<sup>18</sup> Perovskites also show promise as light emitters in displays due to the low material cost, facile wavelength tunability, high PLQY, and very narrow emission spectra, allowing them to achieve a wide color gamut.<sup>22,19</sup> However, perovskites in humid or high-temperature environments are vulnerable to the decomposition of the perovskite crystals.<sup>13</sup> Perovskite stability can be improved by covering the surface with organic ligands forming colloidal NCs, preventing water and oxygen from permeating.<sup>2</sup> These can be further enhanced using various strategies, such as forming an inorganic shell or NC/polymer composites; however, they still showed limited stability and needed complex processes to prevent aggregation of NCs in the matrices.<sup>20</sup> In addition, development of stable PNCs under severe conditions (polar chemicals and high temperature with high humidity) are needed for practical applications.

Using in-situ sol-gel processes, chemically encapsulated PNCs via siloxane matrix (CPN) were fabricated, which also showed excellent uniformity similar to previous reports<sup>8-10,13</sup> (Figure 6A). Stability of

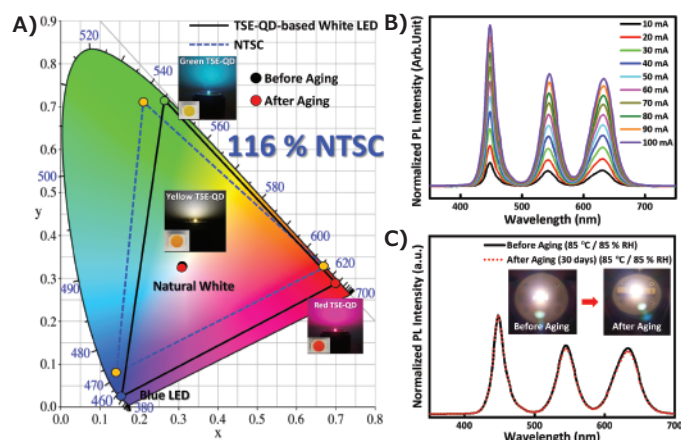


**Figure 5.** A) CIE color coordinates of Blue LED, red TSE-QD, Green TSE-QD, and TSE-QD-based white LED. B) PL spectra of TSE-QD-based white LED as a function of forward bias current from 10 to 100 mA. C) PL intensity before and after reliability test at 85 °C/85% RH. Reprinted with permission from reference 9, copyright 2016 American Chemical Society.

the CPN was investigated, confirming tracing PLQY under various contained humid environments. To our surprise, the CPN exhibited a significantly increasing PLQY, which was maintained for >1.5 years (600 days) under RT ambient air, even in water (Figure 6B). This indicates the recovered optical properties by water.<sup>8-10,13</sup> CPN aged under 85 °C/85% RH also showed similar behavior where PLQY was gradually increased, retaining its value for >100 days (Figure 6C). In a chemical stability test using a strong acid (0.1 M HCl) and base (0.1 M NaOH) (Figure 6D) as well as various polar solvents (ethylene glycol and ethanol) (Figure 6E), recovering optical properties and long-term stability were also confirmed. These results indicate that our CPN has extraordinary-long stability under harsh thermal and chemical environments.

To demonstrate the feasibility of CPN as a color-converting layer in displays, a large area (10 cm x 10 cm) flexible green emissive film was fabricated, showing excellent blue-to-green conversion of light emitted from a mobile phone screen (Figure 7A, left) and stable operation under various bending states (Figure 7A, right). The white-emitting LED integrated with red-emissive Cd-based QDs also exhibited excellent blue-to-white conversion of light emitted from a blue LED chip (Figure 7B, left) and stable color converting properties under various bending states (Figure 7B, right). The CPN-based color converting film and white LEDs showed a wide color gamut (MAPbBr<sub>3</sub>-based CPN: 120% of NTSC 1931 and 89% of Rec. 2020; CsPbBr<sub>3</sub>-based CPN: 130% of NTSC 1931 and 97% of Rec.2020), with higher optical performance than Cd-based QDs (Figure 7C), and excellent stability for >400 days (Figure 7D). Furthermore, water- and chemical-persistent CPNs are highly biocompatible materials, as confirmed by the cell proliferating test using a water-based medium (increased optical density means well-proliferated cells, Figure 7E); these results indicate that the siloxane matrix effectively prevents the toxicity from toxic elements (Cd and Pb). By combining various results, the CPN can enable the use of PNCs in highly stable luminescent materials for display devices and bio-related applications.



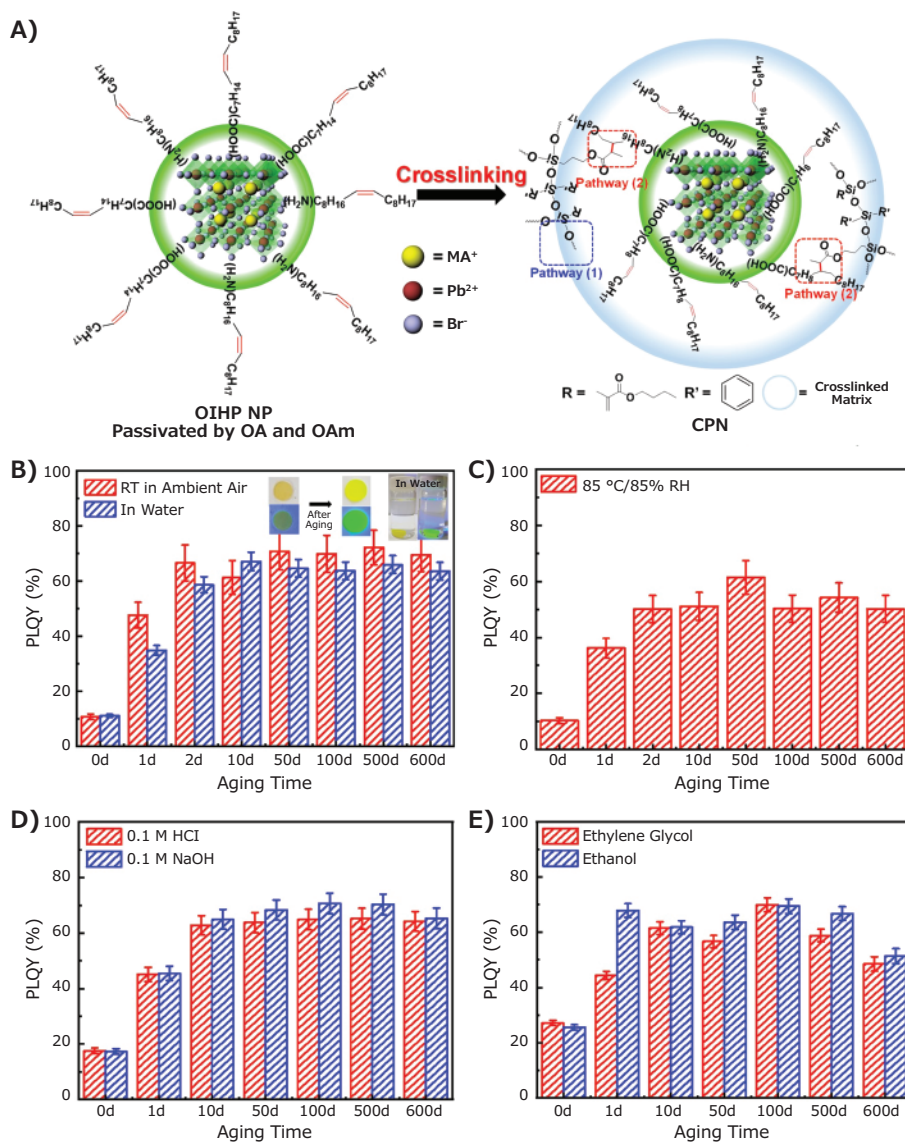


**Figure 6.** A) Schematic illustration of CPN formation. (B–E) Stability of CPN under harsh conditions. PLQY of CPNs **B)** under ambient air at RT and in water, **C)** under 85 °C/85% RH, **D)** in acid and base solutions, and **E)** in ethylene glycol and ethanol. Reprinted with permission from reference 14, copyright 2021 Elsevier.

## Conclusion

We have developed a simple and effective materials design strategy for improving the stability of luminescent NCs against heat, moisture, light, and chemicals via in-situ sol-gel synthesized encapsulation method via siloxane matrix at the molecular scale. The chemical crosslinking between surface ligands on NCs and organic functional groups of the siloxane matrix induces uniform distribution and enhances stability; the resulting composites showed outstanding stability of luminescent NCs in various harsh conditions. In addition, siloxane hybrid materials increased the stability of different types of luminescent NCs, which means that our wavelength converting platform approach to fabricate NC-dispersed nanocomposite designs enables diverse applications. Our materials design strategy can trigger immense research to promote commercialization of luminescent NCs for actual applications to optoelectronics and bio-related applications that require high stability under various severe environmental conditions.

## References

- (1) Kim, J. Y.; Voznyy, O.; Zhitomirsky, D.; Sargent, E. H. *Adv. Mater.* **2013**, *25*, 4986.
- (2) Kim, Y.-H.; Wolf, C.; Kim, Y.-T.; Cho, H.; Kwon, W.; Do, S.; Sadhanala, A.; Park, C. G.; Rhee, S.-W.; Im, S. H.; Lee, T.-W. *ACS Nano* **2017**, *11*, 6586.
- (3) Rabouw, F. T.; Kamp, M.; van Dijk-Moes, R. J.; Gamelin, D. R.; Koenderink, A. F.; Meijerink, A.; Vanmaekelbergh, D. *Nano Lett.* **2015**, *15*, 7718.
- (4) Mehta, A.; Im, J.; Kim, B. H.; Min, H.; Nie, R.; Seok, S. I. *ACS Nano* **2018**, *12*, 12129.
- (5) Lee, H.; Kim, J.; Kim, H.; Kim, J.; Kwon, S. *Nat. Mater.* **2010**, *9*, 745.
- (6) Moon, H.; Lee, C.; Lee, W.; Kim, J.; Chae, H. *Adv. Mater.* **2019**, *31*, 1804294.
- (7) Kim, D.; Shin, K.; Kwon, S. G.; Hyeon, T. *Adv. Mater.* **2018**, *30*, 1802309.
- (8) Jang, J.; Yoon, D.-E.; Kang, S.-M.; Kim, Y. H.; Lee, I.; Lee, H.; Kim, Y. H.; Lee, D. C.; Bae, B.-S. *Nanoscale* **2019**, *11*, 14887.
- (9) Kim, H. Y.; Yoon, D.-E.; Jang, J.; Lee, D.; Choi, G.-M.; Chang, J. H.; Lee, J. Y.; Lee, D. C.; Bae, B.-S. *J. Am. Chem. Soc.* **2016**, *138*, 16478.
- (10) Kuk, S. K.; Jang, J.; Han, H. J.; Lee, E.; Oh, H.; Kim, H. Y.; Jang, J.; Lee, K. T.; Lee, H.; Jung, Y. S.; Park, C. B.; Bae, B.-S. *ACS Appl. Mater. Interfaces* **2019**, *11*, 15952.
- (11) Li, Z.; Kong, L.; Huang, S.; Li, L. *Angew. Chem. Int. Ed.* **2017**, *56*, 8134.
- (12) Wang, H. C.; Lin, S. Y.; Tang, A. C.; Singh, B. P.; Tong, H. C.; Chen, C. Y.; Lee, Y. C.; Tsai, T. L.; Liu, R. S. *Angew. Chem. Int. Ed.* **2016**, *55*, 7924.
- (13) Jang, J.; Kim, Y. H.; Park, S.; Yoo, D.; Cho, H.; Jang, J.; Jeong, H. B.; Lee, H.; Yuk, J. M.; Park, C. B. *Adv. Mater.* **2021**, *33*, 2005255.

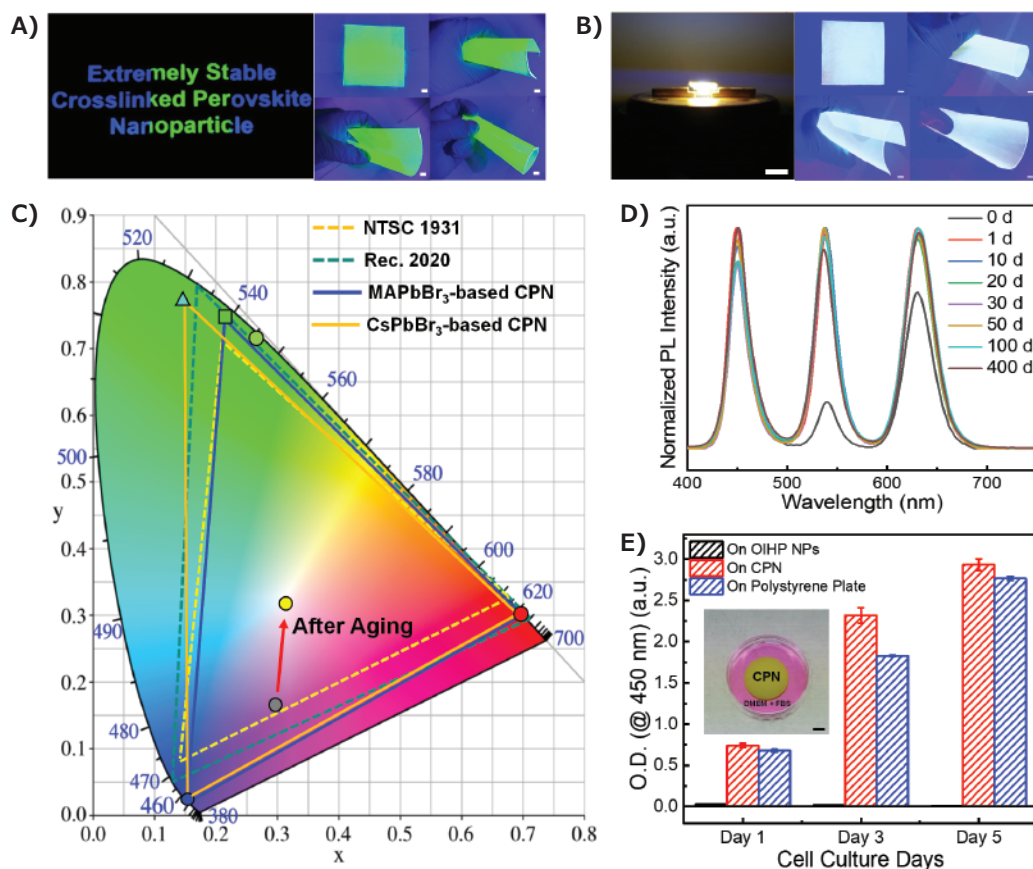


**Figure 7.** Photographs of A) green CPN films on blue-emitting mobile phone screen (*left*), flexible large-area (size: 10 cm × 10 cm) green-emitting CPN films under bending (*right*), B) white LED on blue-LED chip (*left*), and flexible large-area (size: 10 cm × 10 cm) white emitting CPN films under bending (*right*). C) Emission plots of CPN, and white LEDs, NTSC 1931 and Rec.2020 on CIE color coordinates. D) PL spectrum of white LED during stability tests. E) Cell proliferation test results on bare PNCs, CPN and control films after 1, 3, 5 days. Reprinted with permission from reference 14, copyright 2021 Elsevier.

- (14) Jang, J.; Im, H.-G.; Lim, D.; Bae, B.-S. *Compos. Sci. Technol.* **2021**, *201*, 108527.
- (15) Guo, S. H.; Xie, X. J.; Huang, L.; Huang, W. *ACS Appl. Mater. Interfaces* **2016**, *8*, 847.
- (16) Bae, J.-Y.; Kim, Y. H.; Kim, H.-Y.; Lim, Y.-W.; Bae, B.-S. *RSC Adv.* **2013**, *3*, 8871.
- (17) Kim, Y. H.; Koh, S.; Lee, H.; Kang, S.-M.; Lee, D. C.; Bae, B.-S. *ACS Appl. Mater. Interfaces* **2019**, *12*, 3961.
- (18) Yoo, J. J.; Seo, G.; Chua, M. R.; Park, T. G.; Lu, Y.; Rotermund, F.; Kim, Y.-K.; Moon, C. S.; Jeon, N. J.; Correa-Baena, J.-P. *Nature* **2021**, *590*, 587.
- (19) Cho, H.; Jeong, S.-H.; Park, M.-H.; Kim, Y.-H.; Wolf, C.; Lee, C.-L.; Heo, J. H.; Sadhanala, A.; Myoung, N.; Yoo, S.; Lee, T.-W. *Science* **2015**, *350*, 1222.
- (20) Huang, S.; Li, Z.; Kong, L.; Zhu, N.; Shan, A.; Li, L. *J. Am. Chem. Soc.* **2016**, *138*, 5749.

## PDMS-Poly(dimethylsiloxane)

### SYLGARD® Silicone

Name	Description	Size	Cat. No.
SYLGARD® 184	Preweighed monomer and curing agent in convenient blister packs.	10 g clip-pack	<b>761036-5EA</b>
		5 g clip-pack	<b>761028-5EA</b>
SYLGARD® 170 silicone elastomer	Kit is comprised of Base/Curing Agent to be mixed in a 10 (base) :1 (curing agent) ratio by weight for manual mixing. Black liquid (part A), off-white liquid (part B) Viscosity: 3160 cPs (part A), 1110 cPs (part B)	10 cc dual syringe with the static mixer	<b>805998-3EA</b>

### Hydride (H) Terminated PDMS

Name	Structure	Molecular Weight	Viscosity (cSt)	Cat. No.
Poly(dimethylsiloxane), hydride terminated	$\text{H}-\text{Si}(\text{CH}_3)_2-\text{O}-\left[ \text{Si}(\text{CH}_3)_2-\text{O} \right]_n-\text{Si}(\text{CH}_3)_2-\text{H}$	average $M_n \sim 580$	-	<b>423785-50ML</b> <b>423785-250ML</b>
		average $M_n \sim 17,500$	$\sim 500$	<b>482064-100ML</b>
		average $M_n \sim 24,000$	$\sim 1,000$	<b>482145-100ML</b>



## Methyl (CH<sub>3</sub>) Terminated PDMS

Name	Structure	Viscosity (cSt)	Cat. No.
Hexamethyldisiloxane		0.65	469300-50ML 469300-250ML
Poly(dimethylsiloxane)		1.0	469319-50ML
Poly(methylhydrosiloxane)		~3 12-45	482382-20ML 176206-50G 176206-250G

## Hydroxy (OH) Terminated PDMS

Name	Structure	Viscosity	Cat. No.
Poly(dimethylsiloxane), bis(hydroxyalkyl) terminated		100 cP	481246-25ML 481246-100ML
Poly(dimethylsiloxane), hydroxy terminated		~25 cSt ~65 cSt ~750 cSt 2550-3570 cSt 3,500 cSt 18,000-22,000 cSt ~50,000 cSt	481939-100ML 481939-500ML 481955-100ML 481955-500ML 481963-100ML 481963-500ML 432989-100ML 432989-500ML 482161-250ML 432997-100ML 432997-500ML 482005-100ML
Poly(dimethylsiloxane), monohydroxy terminated		~79 cSt	480355-50ML

## Amine (NH<sub>2</sub>) Terminated PDMS

Name	Structure	Molecular Weight	Viscosity (cSt)	Cat. No.
Poly(dimethylsiloxane), bis(3-aminopropyl) terminated		average M <sub>n</sub> ~2,500 average M <sub>n</sub> ~27,000	50 2,000	481688-10ML 481688-50ML 481696-50ML

## Epoxy Terminated PDMS

Name	Structure	Molecular Weight	Viscosity (cSt)	Cat. No.
Poly(dimethylsiloxane), diglycidyl ether terminated		average M <sub>n</sub> ~800	15	480282-50ML 480282-250ML
Poly(dimethylsiloxane), monoglycidyl ether terminated		average M <sub>n</sub> ~5,000	~65	480290-25ML

## Other End Group Functionalized PDMS

Name	Structure	Molecular Weight	Viscosity (cSt)	Cat. No.
Poly(dimethylsiloxane), chlorine terminated		average M <sub>n</sub> ~3,000	~3	481653-50ML
Poly(dimethylsiloxane), vinyl terminated		average M <sub>w</sub> ~25,000	850-1,150	433012-100ML 433012-500ML
Polydimethylsiloxane-diacrylamide		average M <sub>n</sub> 1,200	-	798266-1G

## PDMS-co-polymers

Name	Viscosity (cSt )	Cat. No.
Poly[dimethylsiloxane-co-(3-aminopropyl)methylsiloxane]	~90 at 25 °C	480304-50ML 480304-250ML
Poly(dimethylsiloxane-co-diphenylsiloxane), dihydroxy terminated	~60	482153-25ML
Poly(dimethylsiloxane-co-diphenylsiloxane), divinyl terminated	~500	482048-25ML
Poly[dimethylsiloxane-co-(2-(3,4-epoxycyclohexyl)ethyl)methylsiloxane]	~3,300 at 25 °C	480312-50ML 480312-250ML
Poly[dimethylsiloxane-co-[3-(2-(2-hydroxyethoxy)ethoxy)propyl]methylsiloxane]	75	480320-250ML
Poly(dimethylsiloxane-co-methylphenylsiloxane)	125	378488-50ML
Poly(dimethylsiloxane-co-methylphenylsiloxane)	50	378445-50ML
Poly[dimethylsiloxane-co-methyl(stearoyloxyalkyl)siloxane]	35 at 60 °C	480363-10G

## Other Siloxanes

Name	Form	Description	Cat. No
1,3-Divinyltetramethyldisiloxane	liquid	97%	371904-10G 371904-50G
1,3,5,7,9,11,14-Heptaisobutyltricyclo[7.3.3.15,11]heptasiloxane-endo-3,7,14-triol	powder or crystals	97%	534463-10G
Hexamethyldisiloxane	liquid	viscosity: 0.65 cSt (25 °C)	469300-50ML 469300-250ML
1,3,5,7,9,11-Octaisobutyltetracyclo[7.3.3.15,11]octasiloxane-endo-3,7-diol	powder or crystals	97%	534447-1G
Octamethylcyclotetrasiloxane	liquid	98%	235695-25G 235695-100G
Poly(methylhydrosiloxane)	liquid	average Mn 1,700-3,200	176206-50G 176206-250G
Poly(methylhydrosiloxane), trimethylsilyl terminated	liquid	average Mn ~390	482382-20ML
Poly(methylphenylsiloxane)	viscous liquid	viscosity: 450-550 cSt (25 °C)	378496-50ML

## Alkoxysilanes

Name	Form	Description	Cat. No
11-Acetateundecyltrimethoxysilane	liquid (colorless)	≥95%	SIK4522-20-250MG SIK4522-20-1G
Allyltriethoxysilane	liquid	97%	A36301-5G
3-Aminopropyl(diethoxy)methylsilane	liquid	97%	371890-50ML 371890-250ML
(3-Aminopropyl)triethoxysilane	liquid	99%	40140-100ML 440140-500ML
(3-Aminopropyl)trimethoxysilane	liquid	97%	281778-5ML 281778-100ML 281778-500ML
11-Azidoundecyltriethoxysilane	liquid (colorless)	≥95%	SIK4711-30-250MG SIK4711-30-1G
Bis(3-(methylamino)propyl)trimethoxysilane	liquid		555150-25ML
(Chloromethyl)triethoxysilane	liquid	96%	391042-5G
(Chloromethyl)trimethoxysilane	liquid	96%	597201-25G
3-Cyanopropyltriethoxysilane	liquid	98%	374156-25G 374156-100G
Diethoxydimethylsilane	liquid	97%	175595-100ML 175595-500ML
Diethoxydiphenylsilane	liquid	97%	D83532-50ML
Diethoxy(methyl)vinylsilane	liquid	97%	259462-25G
Dimethyl-di(methacroyloxy-1-ethoxy)silane	liquid	>90.0%	799173-5G
Diphenylsilanediol	powder	95%	D213705-100G
Ethoxytrimethylsilane	liquid	98%	254371-25G 254371-100G
3-Glycidoxypropyldimethoxymethylsilane	liquid	97%	539252-25ML
3-Glycidoxypropyldimethylethoxysilane	liquid	97%	539260-25ML
(3-Glycidylloxypropyl)trimethoxysilane	liquid	≥98%	440167-100ML 440167-500ML 440167-1L 440167-2.5L
12,12,13,13,14,14,15,15,16,16,17,17,18,18,19,19,19-Heptafluoroundecyltriethoxysilane	liquid	98%	SIK4113-30-250MG SIK4113-30-1G
3-Methacrylamidopropyltris(trimethylsiloxy)silane	liquid	>95%	900651-1G
(3-Methacroyloxy-2-hydroxypropoxy)propylbis(trimethylsiloxy)methylsilane	liquid	95%	900650-1G
Methoxytrimethylsilane	liquid	99%	253006-25G 253006-100G 253006-250G

Name	Form	Description	Cat. No
12,12,13,13,14,14,15,15,15-Nonafluoropentadecyltriethoxysilane	liquid	95%	SIK4120-30-250MG SIK4120-30-1G
mPEG20K-Silane	solid	average Mn 20,000	JKA3100-1G
mPEG5K-Silane	solid	average Mn 5,000	JKA3037-1G
11-Pentafluorophenoxyundecyltrimethoxysilane	liquid (colorless)	≥95%	SIK4404-20-250MG SIK4404-20-1G
1H,1H,2H,2H-Perfluorodecyltriethoxysilane	liquid	97%	658758-5G 658758-25G
Poly(N-isopropylacrylamide) triethoxysilane terminated	solid	average Mn 5,000	760978-1G 760978-5G
12,12,13,13,14,14,15,15,16,16,17,17,17-Tridecafluoroheptadecyltriethoxysilane	liquid	95%	SIK4117-30-250MG SIK4117-30-1G
12,12,13,13,14,14,15,15,16,16,17,17,17-Tridecafluoroheptadecyltrimethoxysilane	liquid	95%	SIK4116-20-250MG SIK4116-20-1G
Triethoxyvinylsilane	liquid	97%	175560-100ML 175560-500ML
Trimethoxy(octyl)silane	liquid	96%	376221-25ML
Trimethoxy(2-phenylethyl)silane	liquid	98%	438340-1G
Trimethoxyphenylsilane	liquid	97%	104744-50ML 104744-250ML
Tris(2-methoxyethoxy)(vinyl)silane	liquid	98%	175587-100ML
Vinyltrimethoxysilane	liquid	98%	235768-100ML 235768-500ML

## Silicon Alkoxides

Name	Form	Purity	Cat. No
n-Propyltriethoxysilane	liquid	≥98%	679321-50G
Tetrabutyl orthosilicate	liquid	97%	T5702-100G
Tetraethyl orthosilicate	liquid	99.999% trace metals basis	333859-25ML 333859-100ML
	liquid	98%	131903-25ML 131903-250ML 131903-500ML
	liquid	≥99.5%, GC	759414-25ML
	liquid	≥98% ≥99.9% trace metals basis	679259-50G
Tetramethyl orthosilicate	liquid	≥99%	341436-25G 341436-100G
	liquid	98%	218472-100G 218472-500G
	liquid	≥98%	679240-50G
Tetrapropyl orthosilicate	liquid	≥98%	679240-50G
	liquid	95%	235741-100G

## Silanes

Name	Form	Purity	Cat. No
Azidotrimethylsilane	liquid	95%	155071-10G 155071-50G
Di-n-octyldichlorosilane	liquid	98%	768758-1G
9,9-Dioctyl-9H-9-silafluorene-2,7-bis(boronic acid pinacol ester)	liquid	97%	760102-500MG
Hexachlorodisilane	liquid	96%	205184-5G 205184-25G
	liquid	20% solution in xylene	901482-1L
5-Norbornen-2-yl(ethyl)chlorodimethylsilane, mixture of endo and exo	liquid	95%	544337-1ML
Octenyltrichlorosilane, mixture of isomers	liquid	96%	539279-25ML
Tetrakis(4-bromophenyl) silane	powder	≥96%	914037-1G
Trichloro(dichloromethyl)silane	liquid	96%	479039-25ML
Trichlorocyclopentylsilane	liquid	95%	446181-25ML
Trichloro(1H,1H,2H,2H-perfluorooctyl)silane	powder	97%	448931-10G
Trichloro(phenethyl)silane	liquid	95%	420034-1G
Trichlorovinylsilane	liquid	97%	104876-100G 104876-500G

## Perovskite Quantum Dots

Name	Description	Fluorescence Emission, $\lambda_{em}$ (nm)	Cat. No
10 mg/mL in toluene	oleic acid and oleylamine coated	480	900747-5ML
	oleic acid and oleylamine coated	450	900748-5ML
	oleic acid and oleylamine coated	530	905062-5ML
	oleic acid and oleylamine coated	510	900746-5ML

## CdS/ZnS

Name	Description	Fluorescence Emission, $\lambda_{em}$ (nm)	Cat. No
1 mg/mL in H <sub>2</sub> O, powder	carboxylic acid	540	900221-1ML
	carboxylic acid	580	900222-1ML
	carboxylic acid	600	900223-1ML
	carboxylic acid	620	900224-1ML
	carboxylic acid	560	900225-1ML
	carboxylic acid	645	900226-1ML
1 mg/mL in H <sub>2</sub> O, dispersion	carboxylic acid functionalized	520	900248-1ML
	4 $\mu$ M in 10 mM PBS, amine	540	900235-250UL
	4 $\mu$ M in 10 mM PBS, amine	520	900229-250UL
	4 $\mu$ M in 10 mM PBS, amine	560	900236-250UL
	4 $\mu$ M in 10 mM PBS, amine	580	900237-250UL
4 $\mu$ M in H <sub>2</sub> O, dispersion	PEG	580	900246-250UL
	PEG	520	900243-250UL
dispersion	4 $\mu$ M in 10 mM PBS, amine	645	900241-250UL
	4 $\mu$ M in 10 mM PBS, amine	620	900239-250UL
	4 $\mu$ M in 10 mM PBS, amine	600	900238-250UL
4 $\mu$ M in H <sub>2</sub> O, dispersion	PEG	620	900247-250UL

# FlexAbility!

Our wide range of printed electronic products, from inks to substrates, enable your creation to come alive. We offer printable inks at various viscosities and particle size, and flexible/rigid substrates with various sizes and thicknesses.

- Conductive Inks
- Semiconductor Inks
- Dielectric Inks
- Substrates

Explore our full product list, please visit [SigmaAldrich.com/PrintedElectronics](http://SigmaAldrich.com/PrintedElectronics)



The life science business of Merck operates as MilliporeSigma in the U.S. and Canada.

**Sigma-Aldrich**<sup>®</sup>  
Lab & Production Materials

**MERCK**



# It's Anhydrous ... It's a Bead ... It's... AnhydroBeads™ Salts

**Our comprehensive portfolio of AnhydroBeads™ salts reduce the uptake rate of environmental moisture for a wide range of technical synthesis applications.**

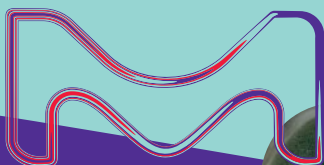
AnhydroBeads™ salts are produced and tested under stringent dry manufacturing conditions to ensure optimal quality, with water content at the parts-per-million scale and trace metal purity of 99.9% (3N) to 99.999% (5N).

Due to AnhydroBeads™ salts low surface area-to-volume ratio at ~2 mm in diameter, issues typically associated with crystalline powders, such as caking, clogging, dusting, settling, and static buildup, are minimized, enabling high-performance in pneumatic loading.

**We'll keep your work flowing with AnhydroBeads™ salts!**

**[SigmaAldrich.com/anhydrobeads](https://SigmaAldrich.com/anhydrobeads)**

The life science business of Merck operates as MilliporeSigma in the U.S. and Canada.



**Features and Benefits:**

- Superior performance in air- & moisture-sensitive applications
- Monodisperse and free flowing for easy handling
- Consistent high quality and high purity from batch to batch
- Low volatility for safe and stable use, storage, and transport





# Poly(2-isopropyl-2-oxazoline)-based Multimodal Stimuli-responsive Functional Materials



Kyeong-Im Hong, Chan-ho Shin, Woo-Dong Jang\*

Department of Chemistry, Yonsei University, 50 Yonsei-ro, Seodaemun-gu, Seoul 03722, Korea  
\*Email: wdjang@yonsei.ac.kr

## Introduction

Various exciting phenomena exhibited by stimulus-responsive materials have greatly influenced materials design.<sup>1-3</sup> In particular, temperature-responsive polymeric materials are used as sensors, catalysts, drug delivery systems, and separation media. Poly(2-isopropyl-2-oxazoline) (PiPrOx) is a typical temperature-responsive polymer that shows lower critical solution temperature (LCST) in an aqueous solution.<sup>4-17</sup> At the LCST, the polymer exhibits a hydrophilic-hydrophobic phase transition. PiPrOxs have attracted attention in the biomedical field because the LCST is close to body temperature and nontoxic. Also, PiPrOxs are used as a precursor for linear poly(ethylene imine). Because the preparation of PiPrOxs proceeded by living cationic ring-opening polymerization of 2-isopropyl-2-oxazoline monomer, the average molecular weight and dispersity can be precisely controlled. The narrow molecular weight distribution of PiPrOxs shows rapid thermal transition behavior over a narrow temperature range.

Moreover, the nature of functional end groups significantly affects the LCST of PiPrOxs. The concentration of the PiPrOxs and additives such as salts or surfactants also influence the LCST. Based on the temperature properties of PiPrOxs, we have recently developed several multimodal stimuli-responsive polymeric systems. This review will briefly show recent developments of PiPrOx-based functional stimuli-responsive polymers.

## Preparation and Modification of PiPrOxs

Because PiPrOxs are obtained by living cationic ring-opening polymerization, various functional groups can be easily introduced to the initiation and termination ends (Figure 1). For example, propargyl-bearing clickable PiPrOxs can be prepared using

propargyl tosylate as the functional initiator. Similarly, other functional groups, such as acrylate and boronic ester, can also be introduced to the initiation end. Various functional groups can be introduced by adding a nucleophilic substance to the active terminal of the living chain. For example, azide groups can be introduced to the termination end by treating the reactive chain end of PiPrOxs with sodium azide (Cat. No. 1.06688). If propargyl amine was used as a terminating agent, we could introduce a clickable propargyl group at the termination end of PiPrOxs. By treating with 4,4-bipyridyl (Cat. No. 289426), we obtained redox-active viologen-bearing PiPrOxs. The propargyl and azide groups can be further modified by click or Sonogashira coupling reaction to introduce various functional groups.

## pH Responsive Poly(benzyl ether) Dendron-conjugated PiPrOx

Dendrimers are regularly branched macromolecules that exhibit various unique properties. For example, the solution properties of dendrimers are highly dependent on the nature of surface functionalities. Poly(benzyl ether) dendrimers with peripheral benzoic acid moieties show high solubility in an aqueous medium with a neutral pH, although the benzyl ether building blocks have a hydrophobic nature. A series of dendritic-linear block copolymers (Figure 2; G2-*b*-PiPrOx and G3-*b*-PiPrOx) was synthesized as dual-mode stimuli-responsive polymers via the click reaction between azide functionalized poly(benzyl ether) dendron and propargyl-bearing PiPrOx.<sup>4,10</sup> Although the pKa value of benzoic acid is about 4.2 in aqueous media, the pKa values of benzoic acid moieties in poly(benzyl ether) dendrimers can be further increased due to neighboring group effect. If one carboxylic acid group was



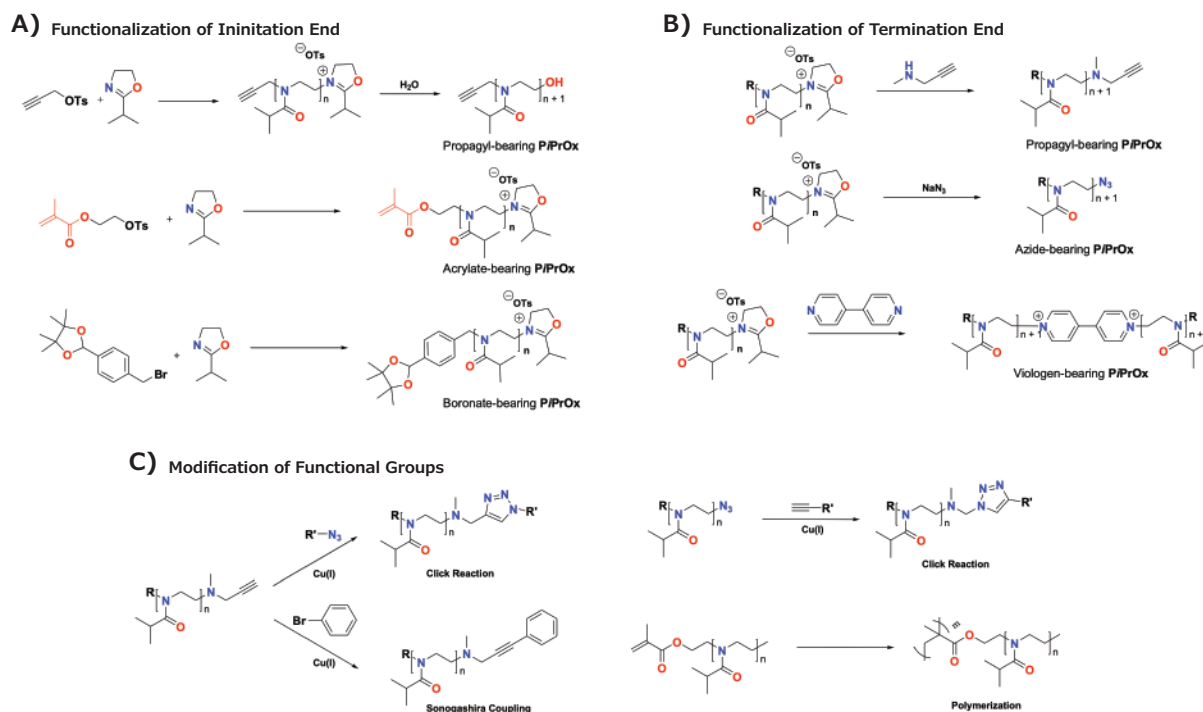


**Figure 1.** Preparation and modification of PIPrOx

deprotonated, the deprotonation of neighboring carboxylic acid could be interfered with by charge repulsion. Such effect resulted in a dramatic change of the cloud point temperature ( $T_{CP}$ ) in response to the pH changes of G2-*b*-PIPrOx and G3-*b*-PIPrOx in an aqueous solution; the  $T_{CP}$  was recorded at a temperature corresponding to a 10% decrease in the optical transmittance by a spectrophotometer. The transmittance changes of G2-*b*-PIPrOx (0.05 mM) and G3-*b*-PIPrOx (0.05 mM) were measured in a 20 mM phosphate buffered solution (PBS, 150 mM NaCl). As the pH decreased, the peripheral carboxylates gradually protonated, and G2-*b*-PIPrOx and G3-*b*-PIPrOx were finally precipitated. As shown in **Figure 2**, the  $T_{CP}$  of G2-*b*-PIPrOx shows changes from 35 to 65 °C between pH ranges from 5.5 to 6.9. The G3-*b*-PIPrOx shows more dramatic  $T_{CP}$  changes from 35 to 83 °C between pH ranges from 5.5 to 6.5. Because the dendritic-linear block copolymers showed pH and temperature-dependent solubility changes, G2-*b*-PIPrOx and G3-*b*-PIPrOx formed different types of self-assembled structures by changing pH and temperature. For example, G2-*b*-PIPrOx and G3-*b*-PIPrOx formed fibrous assemblies at low pH and temperatures. Alternatively, a sheet-like structure was observed for G3-*b*-PIPrOx at high temperature and pH conditions.

### Photo-responsive PIPrOx

The propargyl-bearing telechelic PIPrOx was modified to azobenzene-bearing PIPrOx (**Figure 3A**, Az-PIPrOx-Az) via Sonogashira coupling reaction. Az-PIPrOx-Az showed reversible *cis-trans* photoisomerization of azobenzene units under 365 or 254 nm UV irradiation.<sup>9</sup> Upon 365 nm UV irradiation, the  $T_{CP}$  of Az-PIPrOx-Az was slightly increased by photoisomerization of azobenzene groups due to the polarity change of end functional groups. The azobenzene moiety can form a host-guest complex

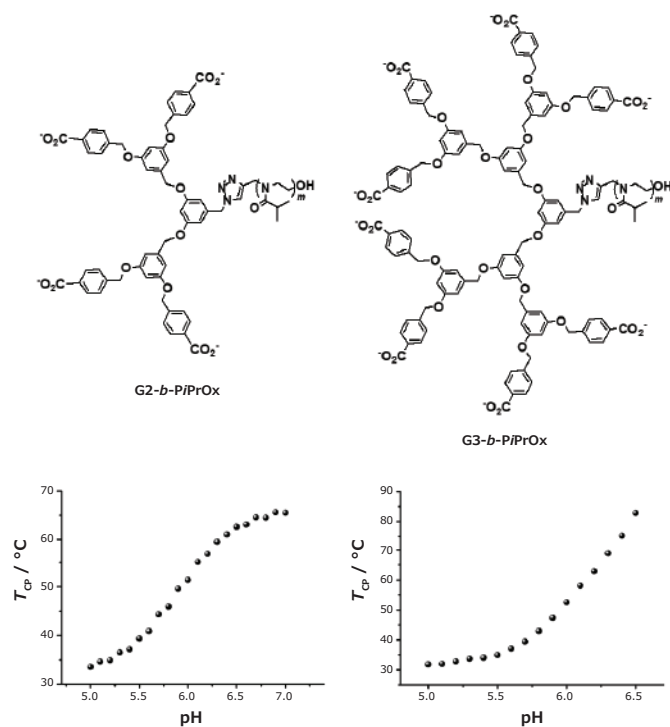


**Figure 2.** Structure of dendritic-linear block copolymers (G2-*b*-PIPrOx and G3-*b*-PIPrOx) with pH-dependent  $T_{CP}$  changes. Reproduced with permission of The Royal Society of Chemistry.

with cyclodextrin (CD). Both *trans*- and *cis*-azobenzene moieties can be accommodated in the  $\beta$ -CD, but the *cis*-azobenzene cannot be adapted to  $\alpha$ -CD due to its small cavity size (i.e., 0.57 nm). When the azobenzene moieties are bound to CDs, the end

functional groups can be changed to a more hydrophilic state. Therefore, the  $T_{CP}$  of Az-*PiPrOx*-Az was slightly increased by the formation of host-guest complexes with  $\alpha$ -CD and  $\beta$ -CD. After the formation of host-guest complexes, 365 nm UV light was irradiated to the Az-*PiPrOx*-Az solutions to induce *trans* to *cis* photoisomerization. As a result, the  $T_{CP}$  of the Az-*PiPrOx*-Az with  $\alpha$ -CD and  $\beta$ -CD moved in opposite directions. Upon the 365 nm UV light irradiation,  $\alpha$ -CD can be released from the host-guest complex. After photoisomerization, the  $\beta$ -CD with large cavities were more tightly bound to the *cis*-azobenzene moiety. The tight binding of *cis*-azobenzene to  $\beta$ -CD influences the  $T_{CP}$  of Az-*PiPrOx*-Az. Using these properties, we controlled the solubility of Az-*PiPrOx*-Az by UV irradiation at a specific temperature. The transparent solution of Az-*PiPrOx*-Az with  $\alpha$ -CD at 25 °C becomes turbid under 365 nm irradiation. Alternatively, the turbid solution of Az-*PiPrOx*-Az with  $\alpha$ -CD became transparent under 254 nm irradiation Az-*PiPrOx*-Az also achieved the opposite with  $\beta$ -CD at 28 °C.

Azobenzene was used to photochemically control  $T_{CP}$  of *PiPrOx* derivatives.<sup>12</sup> We prepared  $\alpha$ -CD-bearing telechelic *PiPrOx* (Figure 3B, CD-*PiPrOx*-CD) as the host for azobenzene derivatives. The  $T_{CP}$  of CD-*PiPrOx*-CD (2.0 g L<sup>-1</sup>) in 10 mM PBS solution (150 mM NaCl, pH 7.4) was displayed at 42.9 °C upon addition of the azobenzene-bearing penta(ethylene glycol) (Az-5EG) (3.3 mM) the  $T_{CP}$  dramatically changed to 8.5 °C. At 365 nm irradiation, the

$T_{CP}$  changed to 41.3 °C, indicating the release of Az-5EG. The  $T_{CP}$  changes were fully reversible during alternate irradiation at 365 and 254 nm.

### Cyclic *PiPrOx*s

Because propargyl and azide groups can be introduced to the initiation and termination ends, cyclic *PiPrOx* (Figure 3C, *c-PiPrOx*) can be prepared through an intramolecular click reaction.<sup>6</sup> When compared to linear *PiPrOx* (Figure 3C, *l-PiPrOx*) with the same molecular weight and dispersity, *c-PiPrOx* showed much higher  $T_{CP}$ . The  $T_{CP}$  of *l-PiPrOx* displayed photosensitivity at 43.4, 45.9, and 50.6 °C for 5.0, 3.0, and 1.0 g/L, respectively. In the case of *c-PiPrOx*, the  $T_{CP}$  appeared at 56.3, 60.2, and 69.0 °C for 5.0, 3.0, and 1.0 g/L, respectively. When the *c-PiPrOx* and *l-PiPrOx* were mixed, the  $T_{CP}$  was gradually increased as the contents of *c-PiPrOx* increased. Using this property, we could precisely control the thermal transition temperature by changing the mixing ratio.

We also prepared azobenzene-containing linear and cyclic *PiPrOx*s (Figure 3D, *l-Az-PiPrOx* and *c-Az-PiPrOx*, respectively) to control  $T_{CP}$  photochemically.<sup>7</sup> As expected, the photoisomerization of the azobenzene moiety resulted in the change of the  $T_{CP}$  of the polymers. *Cis* isomers exhibited a higher thermal transition temperature than *trans* isomers.

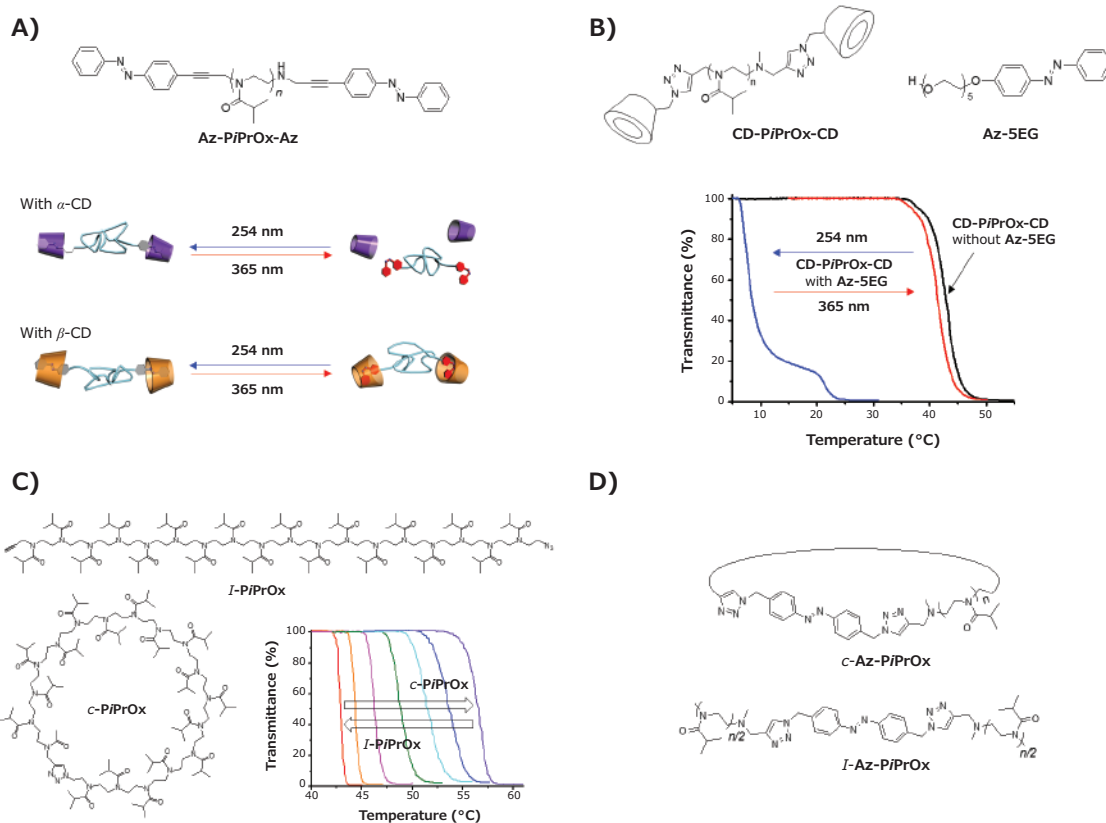


**Figure 3.** A) Structure of Az-*PiPrOx*-Az and photo-responsive host-guest complexation of Az-*PiPrOx*-Az with cyclodextrins. B) Structures of CD-*PiPrOx*-CD and Az-5EG with photo-responsive temperature-dependent transmittance changes. C) Structures of *l-PiPrOx* and *c-PiPrOx* with temperature-dependent transmittance changes of *l-PiPrOx* and *c-PiPrOx* mixtures. D) Structures of *l-Az-PiPrOx* and *c-Az-PiPrOx*. Reproduced with permission of The Royal Society of Chemistry and The American Chemical Society.

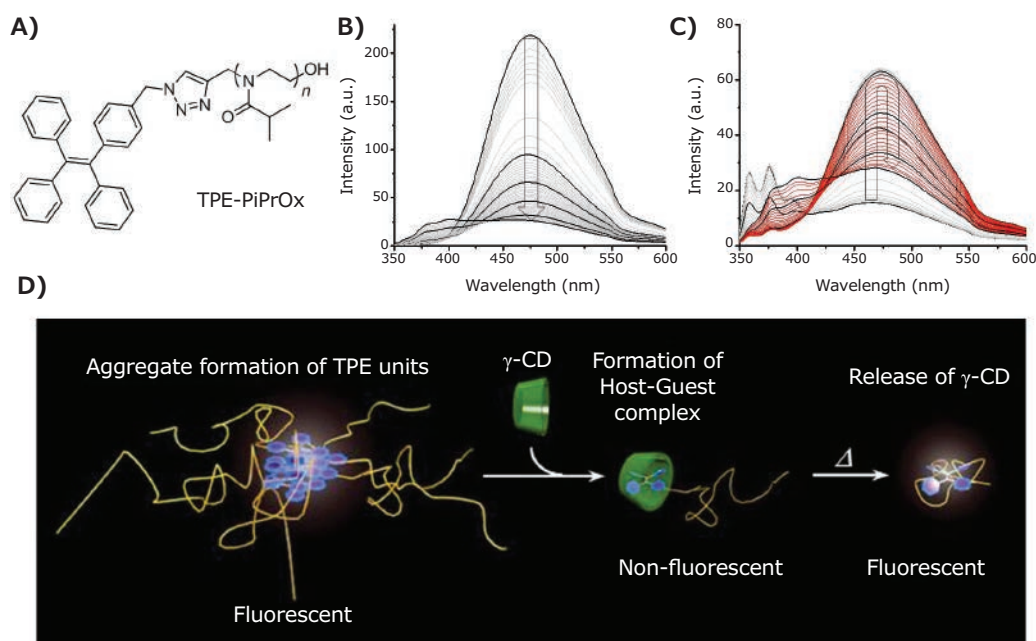


**Figure 4.** A) Structure of TPE-PiPrOx, B) fluorescence emission ( $\lambda_{\text{ex}} = 310$  nm) spectra of TPE-PiPrOx (50  $\mu\text{M}$  in 10mM PBS, pH 7.4) and C) TPE-PiPrOx with  $\gamma$ -CD (20 eq) upon heating from 25 to 70  $^{\circ}\text{C}$ . D) The picture describes the host-guest complex of the TPE-PiPrOx with  $\gamma$ -CD and thermal transition. Reproduced with permission of The Royal Society of Chemistry.

### Fluorescent Dye-conjugated PiPrOx

Tetraphenylethene (TPE), a well-known aggregation-induced emission (AIE) unit, was introduced to PiPrOx (Figure 4, TPE-PiPrOx) through the click reaction between azide-bearing TPE and propargyl-bearing PiPrOx.<sup>11</sup> The TPE-PiPrOx exhibited strong fluorescence due to the formation of a micellar structure in an aqueous solution. As the temperature increased, the fluorescence intensity of TPE-PiPrOx gradually decreased due to the thermal relaxation of the excited state. Interestingly, the fluorescence emission of TPE-PiPrOx completely disappeared with the addition of  $\gamma$ -CD, indicating inclusion of the TPE unit into the cavity of  $\gamma$ -CD. The emission of TPE-PiPrOx with  $\gamma$ -CD increased by thermal transition of the PiPrOx chain. Above  $T_{\text{CP}}$ , the hydrophobic PiPrOx chain could be associated with TPE units to expel  $\gamma$ -CD from TPE-PiPrOx.

Three primitive color-emitting dyes, pyrene, boron-dipyrromethene (BODIPY), and porphyrin, were conjugated with azide-bearing PiPrOx to obtain Dye-PiPrOx (Figure 5, B-PiPrOx, G-PiPrOx, and R-PiPrOx).<sup>8</sup> Each Dye-PiPrOx exhibited strong fluorescence emission in the aqueous phase. The  $T_{\text{CP}}$  of B-PiPrOx, G-PiPrOx, and R-PiPrOx appeared around 47, 43, and 39  $^{\circ}\text{C}$ , respectively. Above  $T_{\text{CP}}$ , the emission color of B-PiPrOx was slightly changed from blue to greenish white due to the partial formation of excimer. On the other hand, the emission of G-PiPrOx was completely quenched above  $T_{\text{CP}}$ . Although the emission intensity of R-PiPrOx gradually decreased by increasing temperature, the red emission remained about 20% even above  $T_{\text{CP}}$ . Since Dye-PiPrOx emit three primary colors, a variety of colors can be created by combining them. Moreover, the emission color was varied by temperature changes. For example, the mixture solution of

B-PiPrOx ( $1.0 \times 10^{-6}$  M) and G-PiPrOx ( $1.0 \times 10^{-6}$  M) showed blue emission at room temperature. As temperature increases, the mixture solution's blue emission gradually changes to green color. Moreover, both blue and green colors appeared from the solution under temperature gradient. The ternary mixture solution of B-PiPrOx ( $0.1 \times 10^{-6}$  M), G-PiPrOx ( $0.5 \times 10^{-6}$  M), and R-PiPrOx ( $5 \times 10^{-6}$  M) initially showed white emission which gradually changed to blue and red. When the mixing ratio was changed to B-PiPrOx ( $0.5 \times 10^{-6}$  M), G-PiPrOx ( $4 \times 10^{-6}$  M), and R-PiPrOx ( $3 \times 10^{-6}$  M), the initial green emission gradually changed to blue and finally changed to red.

### Chemo-responsive PiPrOx

An uracil-bearing telechelic PiPrOx (Figure 6, U-PiPrOx-U) was synthesized by click reaction between propargyl-bearing PiPrOx and uracil having an azide group.<sup>14</sup> To U-PiPrOx-U, a total 23 kinds of metal ions were added, and the absorption change of the solution was monitored. As a result, only  $\text{Hg}^{2+}$  caused bathochromic absorption shift of the U-PiPrOx-U, indicating the selective binding of  $\text{Hg}^{2+}$  to uracil moiety. The  $T_{\text{CP}}$  of U-PiPrOx-U ( $0.8 \text{ g L}^{-1}$ ) was appeared at 58.1  $^{\circ}\text{C}$ , which gradually decreased to 37.8  $^{\circ}\text{C}$  by addition of  $\text{Hg}^{2+}$ .

As another type of chemo-responsive PiPrOx, a pinacol boronate-bearing telechelic PiPrOx (Figure 6, B-PiPrOx-B) was prepared.<sup>13</sup> Since boronic esters can be exchanged with chemicals having diol groups, the  $T_{\text{CP}}$  change of B-PiPrOx-B was investigated in the presence various saccharides such as maltose, lactose, glucose, sucrose, mannose, galactose, and fructose. As a result, the  $T_{\text{CP}}$  of B-PiPrOx-B increased with the addition of various saccharides. However, the degree of  $T_{\text{CP}}$  changes greatly depended on the

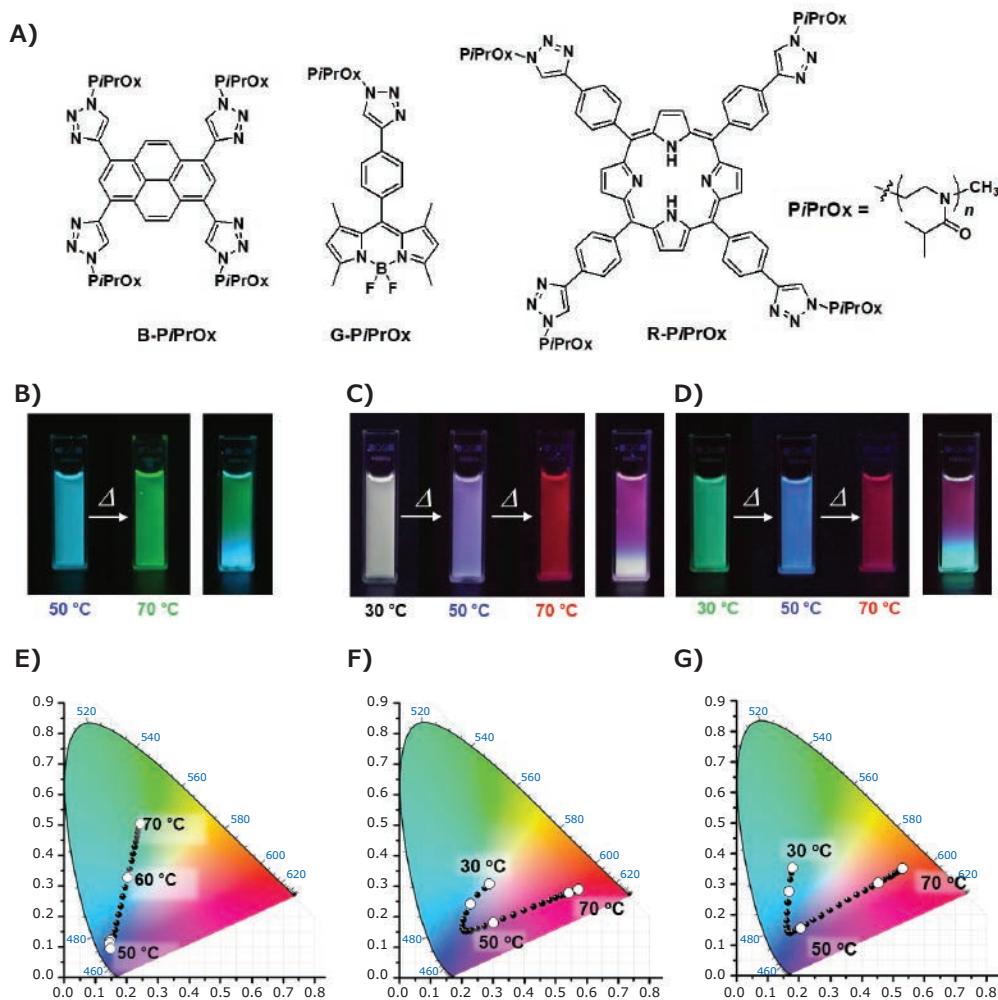


**Figure 5.** A) Structures of Dye-PiPrOxs. Emission color changes of Dye-PiPrOx mixture systems: **B, E**) B-PiPrOx ( $1.0 \times 10^{-6}$  M) and G-PiPrOx ( $1.0 \times 10^{-6}$  M); **C, F**) B-PiPrOx ( $0.1 \times 10^{-6}$  M), G-PiPrOx ( $0.1 \times 10^{-6}$  M), and R-PiPrOx ( $5 \times 10^{-6}$  M); and **D, G**) B-PiPrOx ( $0.5 \times 10^{-6}$  M), G-PiPrOx ( $4 \times 10^{-6}$  M), and R-PiPrOx ( $3 \times 10^{-6}$  M). Reproduced with permission of The Wiley-VCH.

saccharides, where the highest binding affinity has been observed for fructose. Because the solubility of B-PiPrOx-B can be controlled by adjusting the fructose concentration, the design of a fructose-mediated delivery system would be feasible.

### Redox-responsive PiPrOx

A viologen-containing thermo-responsive PiPrOx (Figure 6, PiPrOx-V) was synthesized by treating the active terminal of living polymer with 4,4-bipyridyl.<sup>15</sup> An aqueous solution of PiPrOx-V showed decreasing transmittance by increasing temperature to 50 °C through the hydrophilic-hydrophobic phase transition. With the addition of sodium dithionite, the transparent solution of PiPrOx-V immediately turned blue through the formation of a radical cation by single-electron reduction. The blue color gradually disappeared by aerobic oxidation. Along with the color change, the  $T_{CP}$  of PiPrOx-V was also changed by the redox state change of the viologen unit. Because PiPrOx-V exhibited reversible redox behavior, electrochromic changes were investigated using the sandwich-type ITO glass cell containing an aqueous solution of PiPrOx-V (180 mg/mL) with potassium ferricyanide (20 mM) as an electrolyte. Upon 1.5 V of electric potential applied to the ITO glass cell, the solution turned to violet phase. The violet phase was reversibly changed

to the transparent phase when the applied voltage was removed. The PiPrOx-V-containing ITO glass cell exhibited four different visual states with changes in temperature and electric potential. The thermal and electrochromic changes of PiPrOx-V were fully reversible for 100 cycles of repeated voltage shifts.

### Conclusion

We have briefly introduced several PiPrOx-based functional stimuli-responsive polymeric materials. Since various functional groups can be introduced to both initiation and termination ends of PiPrOx, we could easily combine other types of stimuli-responsive functions with thermo-responsiveness. Moreover, the introduction of propargyl or azide end groups are beneficial for further modification of the PiPrOx. The sharp hydrophilic-hydrophobic thermal transition of PiPrOx is a strong motif for functional polymeric materials and devices. Although most of the examples introduced in this review simply show examples of responding to two different stimuli at the same time, it will be possible to design materials that exhibit structural and functional changes in response to a more significant number of stimuli simultaneously.



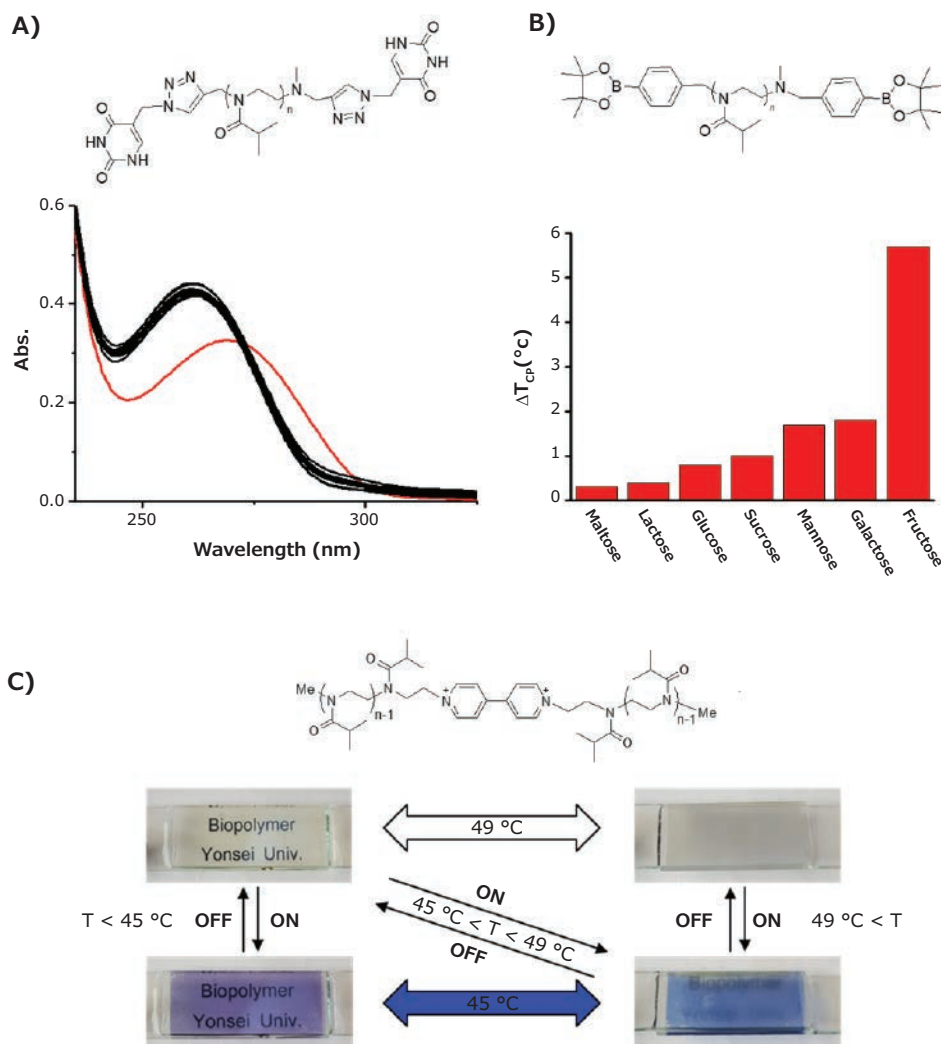


**Figure 6.** A) Structure of U-PiPrOx-U with UV-Vis absorption changes upon addition of various metal ions ( $\text{Hg}^{2+}$ ,  $\text{Ag}^+$ ,  $\text{Al}^{3+}$ ,  $\text{Au}^+$ ,  $\text{Ba}^{2+}$ ,  $\text{Ca}^{2+}$ ,  $\text{Cd}^{2+}$ ,  $\text{Co}^{2+}$ ,  $\text{Cr}^{3+}$ ,  $\text{Cu}^{2+}$ ,  $\text{Fe}^{2+}$ ,  $\text{Fe}^{3+}$ ,  $\text{K}^+$ ,  $\text{Li}^+$ ,  $\text{Mg}^{2+}$ ,  $\text{Mn}^{2+}$ ,  $\text{Na}^+$ ,  $\text{Ni}^{2+}$ ,  $\text{Pb}^{2+}$ ,  $\text{Pt}^{2+}$ ,  $\text{Rh}^{2+}$ ,  $\text{Ru}^{3+}$ , and  $\text{Zn}^{2+}$ ). B) Structure of B-PiPrOx-B with  $T_{cp}$  changes by addition of various sugars. C) Structure of PiPrOx-V with phase transition behaviors by temperature and electric potential changes. Reproduced with permission of The Royal Society of Chemistry.

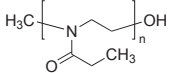
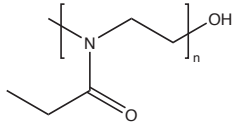
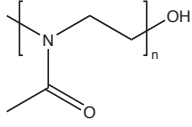
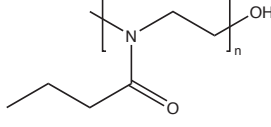
## References

- Jana, S.; Uchman, M. *Prog. Polym. Sci.* **2020**, *106*, 101252.
- Yan, X.; Wang, F.; Zheng, B.; Huang, F. *Chem. Soc. Rev.* **2012**, *41* (18), 6042–6065.
- McConnell, A. J.; Wood, C. S.; Neelakandan, P. P.; Nitschke, J. R. *Chem. Rev.* **2015**, *115* (15), 7729–7793.
- Joe, J. H.; Park, J. M.; Lee, H.; Jang, W.-D. *Eur. Polym. J.* **2019**, *118*, 320–326.
- Jung, Y.; Jang, W.-D. *Supramol. Chem.* **2017**, *29* (10), 714–722.
- Jung, Y.; Kim, J.-H.; Jang, W.-D. *Eur. Polym. J.* **2017**, *88*, 605–612.
- Jung, Y.; Nam, J.; Kim, J.-H.; Jang, W.-D. *RSC Adv.* **2017**, *7* (17), 10074–10080.
- Kim, J. H.; Jung, Y.; Lee, D.; Jang, W. D. *Adv. Mater.* **2016**, *28* (18), 3499–3503.
- Kim, J.-H.; Koo, E.; Ju, S.-Y.; Jang, W.-D. *Macromolecules* **2015**, *48* (14), 4951–4956.
- Kim, J.-H.; Lee, E.; Park, J.-S.; Kataoka, K.; Jang, W.-D. *Chem. Commun.* **2012**, *48* (30), 3662–3664.
- Kim, J.-H.; Yim, D.; Jang, W.-D. *Chem. Commun.* **2016**, *52* (22), 4152–4155.
- Lee, J.; Park, J. M.; Jang, W.-D. *Carbohydr. Polym.* **2019**, *221*, 48–54.
- Lee, J.; Park, J. M.; Jang, W.-D. *Chem. Commun.* **2019**, *55* (23), 3343–3346.
- Nam, J.; Jung, Y.; Jang, W.-D. *Chem. Commun.* **2017**, *53* (81), 11169–11172.
- Nam, J.; Jung, Y.; Joe, J.; Jang, W.-D. *Polym. Chem.* **2018**, *9* (26), 3662–3666.
- Park, J. M.; Kim, Y. J.; Jang, W.-D. *ACS Appl. Polym. Mater.* **2020**, *2* (8), 3535–3542.
- Park, J.-S.; Kataoka, K. *Macromolecules* **2006**, *39* (19), 6622–6630.

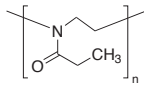
## Oxazolines

Name	Form	Purity	Cat. No
2- <i>n</i> -Butyl-2-oxazoline	Liquid	-	799637-5G
2-Isopropyl-2-oxazoline	Liquid	≥96.5%, GC	799653-5G
2- <i>n</i> -Propyl-2-oxazoline	Liquid	-	799645-5G

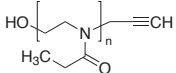
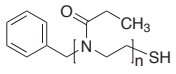
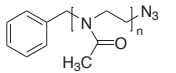
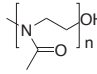
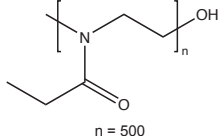
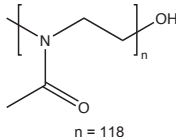
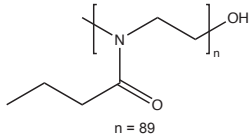
## Low PDI Poly(oxazoline)s

Name	Structure	Molecular Weight (Avg $M_n$ )	PDI	Cat. No
Poly(2-ethyl-2-oxazoline)		5,000	≤1.2	740713-5G
		10,000	≤1.3	741906-5G
		25,000	≤1.4	741884-5G
Ultroxa®: Poly(2-ethyl-2-oxazoline)	 n = 500		≤1.25	900353-1G
Ultroxa®: Poly(2-methyl-2-oxazoline)	 n = 118		≤1.2	900350-1G
Ultroxa®: Poly(2-propyl-2-oxazoline)	 n = 89		≤1.2	900352-1G

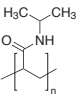
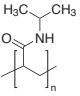
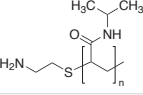
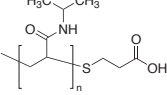
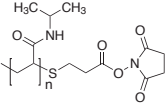
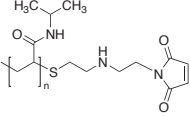
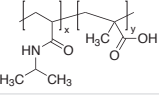
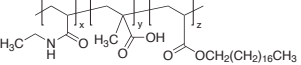
## High Mw Poly(2-ethyl-2-oxazoline)s

Name	Structure	Molecular Weight (Avg $M_n$ )	PDI	Cat. No
Poly(2-ethyl-2-oxazoline)		~50,000	3-4	372846-100G
		~200,000	3-4	372846-500G
		~500,000	3-4	372854-100G
				373974-100G
				373974-500G

## Functionalized Poly(oxazoline)s

Name	Structure	Molecular Weight (Avg $M_n$ )	PDI	Cat. No
Poly(2-ethyl-2-oxazoline), alkyne terminated		2,000	≤1.1	747262-1G
		5,000	≤1.2	778338-1G
Poly(2-ethyl-2-oxazoline), α-benzyl, ω-thiol terminated		2,000	≤1.3	809438-5G
		5,000	≤1.3	900265-5G
		10,000	≤1.3	809446-5G
Poly(2-methyl-2-oxazoline), α-benzyl, ω-azide terminated		2,000	≤1.3	778303-1G
		5,000	≤1.3	778311-1G
Poly(2-methyl-2-oxazoline), hydroxy terminated		2,000	≤1.2	795275-5G
		5,000	≤1.3	795283-5G
Ultroxa®: Poly(2-ethyl-2-oxazoline)	 n = 500	5,000	≤1.15	900360-500MG
		10,000	≤1.2	900359-500MG
		10,000	≤1.2	900357-500MG
		10,000	≤1.2	900355-500MG
Ultroxa®: Poly(2-methyl-2-oxazoline)	 n = 118	10,000	≤1.2	900354-500MG
		10,000	≤1.2	900358-500MG
Ultroxa®: Poly(2-propyl-2-oxazoline)	 n = 89	10,000	≤1.2	900356-500MG

## PNIPAM - Stimuli-Responsive Materials

Name	Structure	Molecular Weight	Cat. No
Poly( <i>N</i> -isopropylacrylamide)		$M_n$ 10,000-15,000	724459-5G
Poly( <i>N</i> -isopropylacrylamide)		$M_n$ 20,000-25,000	535311-10G
Poly( <i>N</i> -isopropylacrylamide), amine terminated		average $M_n$ 2,500	724823-1G 724823-5G
		average $M_n$ 5,500	724831-1G 724831-5G
Poly( <i>N</i> -isopropylacrylamide), carboxylic acid terminated		average $M_n$ 2,000	724815-1G 724815-5G
		average $M_n$ 5,000	724807-1G 724807-5G
		average $M_n$ 7,000	724866-1G 724866-5G
Poly( <i>N</i> -isopropylacrylamide), <i>N</i> -hydroxysuccinimide (NHS) ester terminated		average $M_n$ 2,000	725668-1G 725668-5G
Poly( <i>N</i> -isopropylacrylamide), maleimide terminated		average $M_n$ 2,000	731048-1G 731048-5G
		average $M_n$ 4,000	728632-1G 728632-5G
Poly( <i>N</i> -isopropylacrylamide- <i>co</i> -methacrylic acid)		$M_n$ 40,000-60,000	724467-5G
		$M_n$ 40,000-80,000	724858-5G
Poly( <i>N</i> -isopropylacrylamide- <i>co</i> -methacrylic acid- <i>co</i> -octadecyl acrylate)		$M_n$ 30,000-60,000	724475-5G

# polymers with possibilities

MERCK

## Functionalized Poly(ethylene glycol)s for Drug Delivery

### Polymer of choice for optimal and reproducible results.

When it comes to drug delivery technologies and solutions, poly(ethylene glycol)s or PEGs are the polymer of choice for optimal and reproducible results. With excellent pharmacokinetic properties, they are ideal materials for bioconjugation, pegylation, crosslinking, and hydrogel formation.

Let us help you transform your work into new therapeutic discoveries with our diverse PEG selection.

For a complete list of available materials, visit [SigmaAldrich.com/PEG](http://SigmaAldrich.com/PEG)



# Phyllosilicate Clay Minerals: Principles and Applications



Hansol Ra,<sup>1,2</sup> Sungsoon Kim,<sup>1,2</sup> Taehoon Kim,<sup>1,2</sup> Jihong Bae,<sup>1,2</sup> Wooyoung Shim<sup>1,2\*</sup>

<sup>1</sup> Department of Materials Science and Engineering, Yonsei University, Seoul 120-749, Korea

<sup>2</sup> Center for Multi-Dimensional Materials, Yonsei University, Seoul 03722, Korea

\* E-mail: wshim@yonsei.ac.kr

## Introduction

The emergence of van der Waals materials has opened a spectrum of research exploring two-dimensional (2D) layered materials.<sup>1,2</sup> Inorganic materials with diverse layer types and surface properties have gained attention, including boron nitride, transition metal carbides and nitrides, black phosphorous, and molybdenum disulfide.<sup>3-6</sup> All these materials have strong in-plane chemical bonds but weak out-of-plane van der Waals forces, which allows some of them to be exfoliated into few-layered two-dimensional nanosheets through physical or chemical means.<sup>7-8</sup> Numerous functional materials were reconstructed from 2D nanosheets of these materials, showing high performance and promising results in many fields of science.<sup>8-10</sup>

Clays are abundant in nature and are sustainable; they can be easily modified and show good stability when exposed to high temperatures and acidic environments. As the demand for eco-friendly and cost-effective materials remains high, clays are attractive candidates for next-generation material. Clay minerals are referred to as fine-grained parts of geology composed essentially of hydrous aluminosilicates.<sup>11</sup> Their grain sizes are less than 2  $\mu\text{m}$  in diameter, and most have a phyllosilicate or sheet structure in natural settings. Although clay minerals have a standard structure, diverse transformations in the geometric arrangement of atoms and ions occur within the crystal due to chemical changes or thermal variations while weathering (Figure 1). Thus, numerous members can exist within the same family group with different compositions and properties. Correctly understanding these phyllosilicate materials can open new avenues for diverse functional membranes. Herein, we review recent advances in phyllosilicate materials of the kaolin, mica, smectite, and vermiculite group with a basic understanding of their physical and chemical properties.

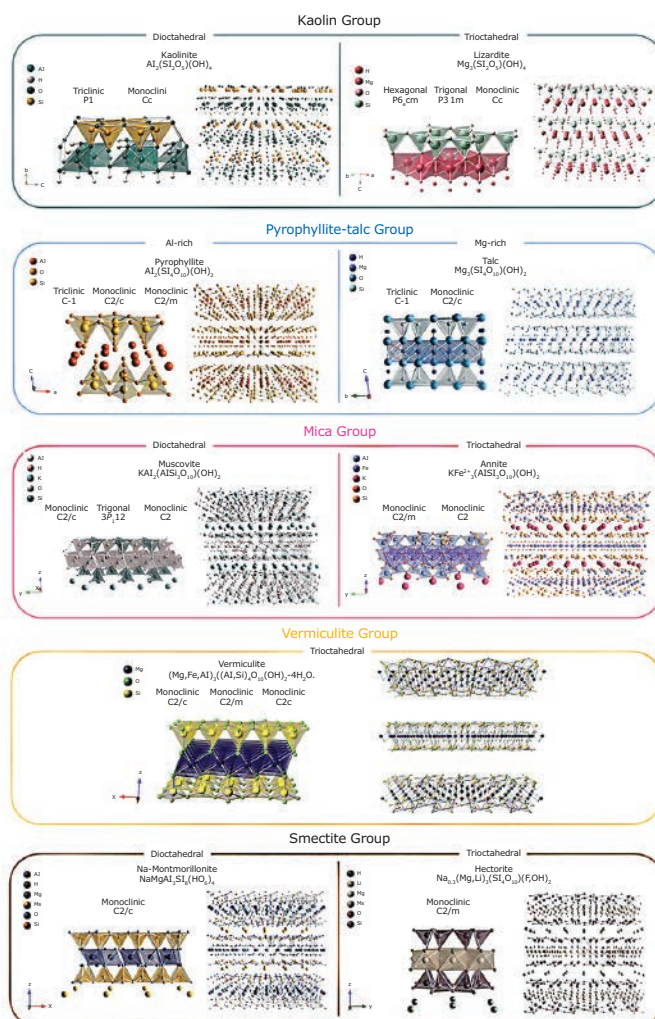


**Figure 1.** Schematics of the crystallographic structure of phyllosilicates in each clay mineralogy groups.

## Phyllosilicates

Phyllosilicates, also called sheet silicates, can be classified according to their structural and molecular arrangement, elemental composition, and swelling properties (Figure 2A).<sup>12</sup> First, clay structure and the arrangements of the molecular units are good standards. As shown in Figure 2B, the foundation of all silicate structures is the silicate tetrahedron (each consisting of a central silicon atom surrounded by four oxygen atoms at the corners of a tetrahedron). The two-dimensional cross-linking of silicon ions and basal oxygens forms the sheet silicate or the phyllosilicate structure. Three basal oxygens are interlinked in such a way as to form a hexagonal-shaped network, and the remaining oxygen is located under the basal plane. The apical oxygen located at the bottom of the sheet can form bonds with other metallic ions. This interlinked metallic ion is coordinated octahedrally. The octahedral polyhedron contains a cation coordinated with six oxygens or hydroxyl units. The linking of tetrahedral and octahedrally coordinated cations is the fundamental characteristic of phyllosilicates. Major basic structural models are 1:1 structure (kaolin group), 2:1 structures (mica, smectite, and vermiculite group), and 2:1 sandwich structure (chlorites). In this review, we will focus on 1:1 and 2:1 structures. Pyrophyllite and talc are used as a model for minerals of dioctahedral (aluminum-rich) and trioctahedral (magnesium-rich) 2:1 structure.

Furthermore, the basic composition of a clay mineral helps us to differentiate phyllosilicates. As mentioned, diverse species of clay minerals can exist due to chemical changes or thermal variations while weathering. Varieties of clays found in nature are formed through equivalent or non-stoichiometric substitutions of cations in the tetrahedral and octahedral sites. One possibility is

a change in the total number of ions present in the octahedral site. The negative charge on a layer silicate unit cell of the tetrahedrally coordinated ions is equivalent to four oxygen ions or eight charges, while the charge on the unit cell of the octahedrally coordinated layer is six or that of three oxygen ions. This leads to two occupancy types of the octahedrally coordinated sites, one with three divalent ions (trioctahedral) or one with two trivalent ions (dioctahedral).

Moreover, diverse pathways such as octahedral, di-trioctahedral, and octahedral-tetrahedral substitutions exist. For example,  $\text{Si}^{4+}$  in the tetrahedral site can be substituted by  $\text{Al}^{3+}$ , and  $\text{Mg}^{2+}$  in the octahedral site can be substituted by  $\text{Fe}^{3+}$  to balance the charge. It is also possible to have an electrostatically balanced interlayer substitution by adding another ion on the surface of the layered sheet of the tetrahedral-octahedral network. Usually, the ion has a charge of +1 or +2, with Na, K, Ca, and Mg the most common ions present (Figure 2B). The trivalent substitution typically causes the interlayer substitution in the tetrahedral site. Substitution in the octahedral site is much rarer. The compositional variation results in different cell dimensions and atomic arrangements due to the charge relations of the polyhedra. Monoclinic shifts caused by the ionic substitutions can produce even more polytypes within the same group.

Lastly, phyllosilicate groups can further be divided by their capacity of clays to swell or to absorb water. Each group has a unique interlayer distance due to its characteristic surface charge (Figure 2C). In the case of kaolins (neutral charge) and micas (high charge), swelling does not occur, whereas smectites and vermiculite groups (both of low charge) swell.

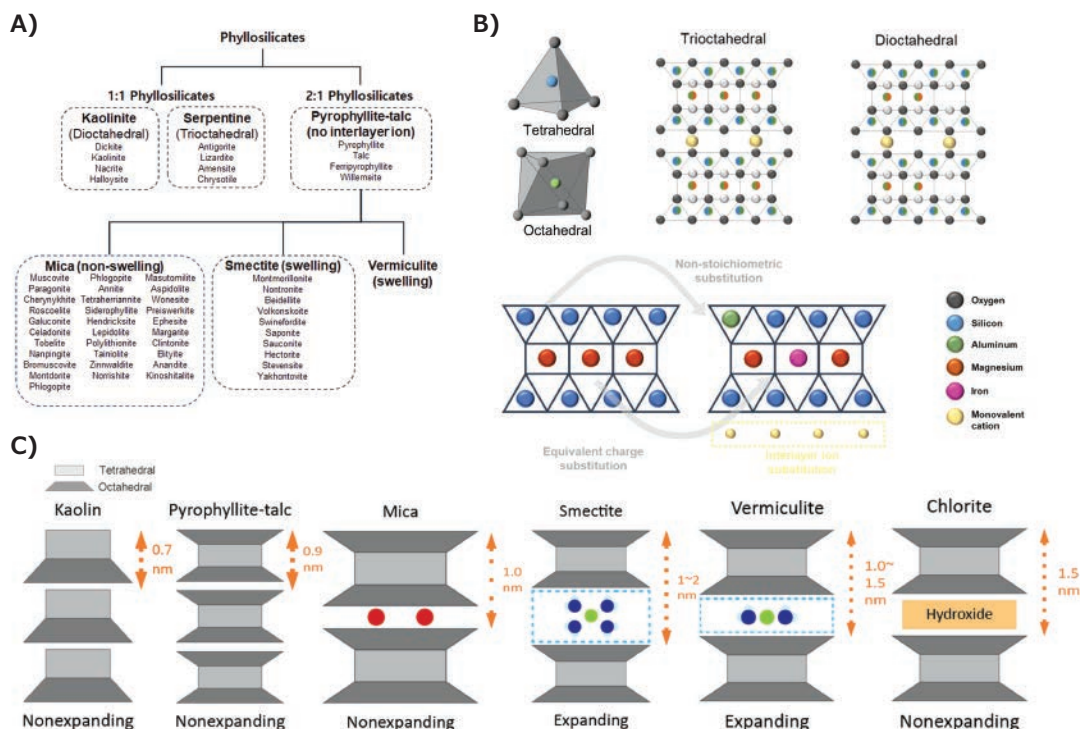


**Figure 2.** Classification of clay mineral groups. A) Relationship between kaolinite, serpentine, pyrophyllite-talc, mica, smectite, and vermiculite group. B) Schematic illustration of trioctahedral and dioctahedral structure with intercalation sites and pathways. C) Schematic illustration of layered structure of each phyllosilicate groups.



## Kaolin Group

The thickness of the tetrahedral-octahedral layers of the kaolin group is around 7 Å.<sup>11</sup> The dioctahedral clays within the kaolin group fall under the kaolinite subgroup and the trioctahedral under the serpentine subgroup. All substitutions within the 1:1 structure result in a neutral lattice; hence, there are no swelling clays within the kaolin family.

The members of the kaolin group serve as important industrial raw materials and have a wide variety of applications in the industry, mainly fillers and coatings. Kaolinite, the most well-known 1:1 clay mineral, has many attractive features for use as a substrate, such as low cost, abundant source, and high mechanical strength.<sup>13</sup> Apart from 2:1 structured phyllosilicate, the layered kaolin structure contains abundant hydroxyl groups in its crystal interlayer and fracture surface, which opens possibilities for diverse chemical modifications.

Zhou et al. reported a surface-rich carboxyl decorated kaolinite composite (PAA-KLN) fabricated through poly(acrylic acid) grafting via an integrated UV-initiated grafting approach (Figure 3A and 3B).<sup>14</sup> Due to the suitable hydrophilic property of poly(acrylic acid) brushes, their free-end would extend into the solution to form a surface villus layer, bringing many highly accessible adsorption

sites. The resultant PAA-KLN exhibited outstanding adsorption capacity for Fe<sup>3+</sup> of 189.63 mg/g and rapid adsorption rate (reaching equilibrium within 40 min) (Figure 3C). Furthermore, PAA-KLN displayed excellent reusability with a high desorption ratio even at a low concentration of stripping liquid (0.2 M HCl), demonstrating its excellent application potential in recycling valuable metal from wastewater (Figure 3D).

Cheng et al. used nano kaolinites to form self-assembled two-dimensional nanofluidic channels by bottom-up construction of kaolinite-based Janus nano-building blocks (Figure 3E).<sup>15</sup> Through an evaporation and vacuum-filtration process, the two-dimensional heterostructures are reassembled into membrane-scale layered materials possessing distinct sub-nanometer and nanometer-wide fluidic channels of about 6.8 and 13.8 Å (Figure 3F). Saturated ionic conductance at low concentrations and the linear relationship of the magnitude of the streaming ionic current with respect to the applied flow rate show similar observations found in the case of a single-channel nanofluidic device (Figure 3G and 3H). Moreover, the output power density from the reconstructed nano kaolinite membranes (RKM) approaches 0.18 W m<sup>-2</sup> and remarkably high mechanical-electric energy conversion compared to GOM (Figure 3I).

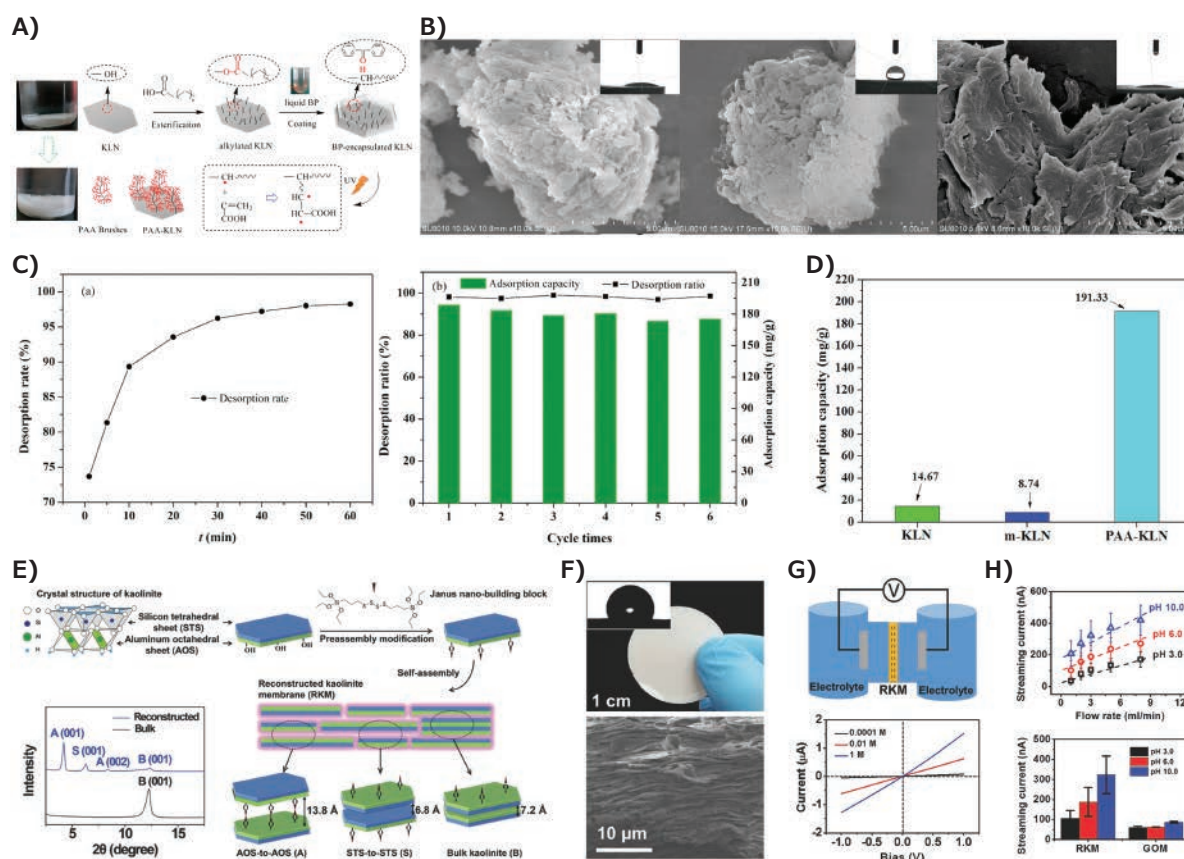


**Figure 3.** Fabrication and performance of kaolinite-based functional membranes. **A)** Scheme of preparation of PAA-KLN adsorbent. **B)** SEM and water contact angle of KLN, m-KLN, PAA-KLN. **C)** Regeneration time and cycle for the evaluation of PAA-KLN performance. **D)** Comparison of adsorption capacities between KLN, m-KLN, and PAA-KLN. Adapted with permission from reference 14, copyright 2018 Elsevier. **E)** Self-assembly and reconstruction of 2D Janus nanosheets with XRD patterns. **F)** Photograph of RKM and SEM observation on the cross-section of the RKM. **G)** Scheme of the experimental setup and representative linear current-voltage responses at different KCl concentrations. **H)** The generated streaming current from RKM at different pH. **I)** The streaming ionic current generated from the RKM compared with GOM at different pH. Adapted with permission from reference 15, copyright 2017 John Wiley and Sons.

## Mica Group

Clay minerals within a mica group have a high charge (0.9–1.0). In micas, there is a charge imbalance due to ionic substitution on the basic 2:1 structure, which is compensated by an interlayer ion, almost uniquely potassium, fixed between the layers and bonding the layers together.<sup>11</sup> Although micas have many attractive properties such as high surface potential, visible-light transparency, ultraviolet-shielding, flexibility, electric thermal insulator, stability in temperature and chemical durability, the exfoliation of single nanosheets with high aspect ratio and layered structure is difficult due to the strong interlayer bonding.<sup>16–17</sup>

In 2015, Jia et al. reported the successful fabrication of self-standing films by exfoliation of stable monolayer muscovite through enlarging the spacing with long-chain OTA<sup>+</sup> (Figure 4A and 4B).<sup>17</sup> Three years later, in 2018, Pan et al. have reported a high-performance biomimetic polymeric mica film with the help of CTA intercalation and ultrasonication in ethanol (Figure 4C).<sup>18</sup> The fabricated film showed fine laminar structure (Figure 4D), excellent mechanical strength (259 MPa and 16.2 GPa with mica content of 60 wt.%), and an as-synthesized device (Figure 4E) showed good conductivity ( $\sim 0.6 \text{ S cm}^{-1}$ ) (Figure 4F) and performance over a wide range of bending angles (Figure 4G).

It makes polymeric mica film a suitable candidate to serve as a novel substrate for flexible and transparent electronic devices, such as photodetectors.

## Smectite Group

The most important and widely known members of the smectite group are montmorillonite, beidellite, nontronite, saponite, and hectorite. They are differentiated by variations in chemical composition involving substitutions in tetrahedral and octahedral sites.<sup>11</sup>

The structure, chemical composition, exchangeable ion type, and small crystal size of smectite clays are responsible for several unique properties, including a large chemically active surface area, high cation exchange capacity, interlamellar surfaces having unusual hydration characteristics, and sometimes the ability to strongly modify the flow behavior of liquids.<sup>19</sup> Different from micas, smectites have a low-charge 2:1 structure (0.2–0.9 charge). Loosely held ions compensate for the net charge imbalance on the tetrahedral-octahedral network in the interlayer position, which can be easily exchanged in solution. Depending on the humidity, the basal spacing can vary from 1 to 2 nm.<sup>12</sup>

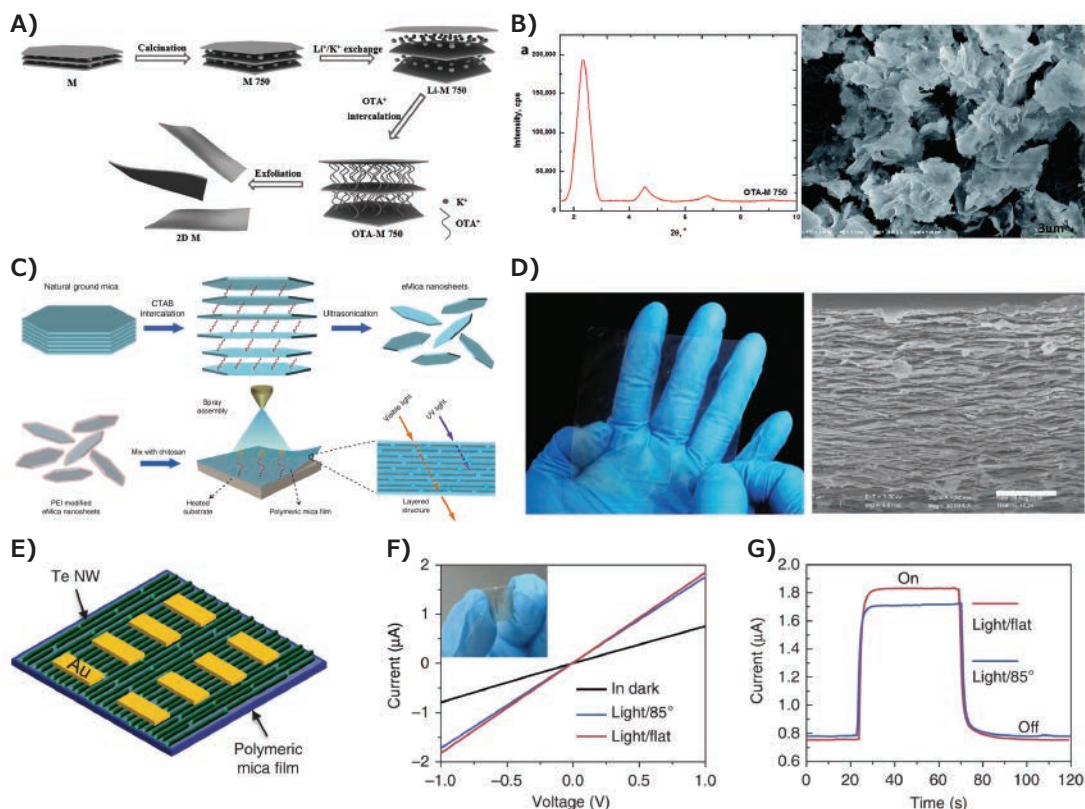


**Figure 4.** Fabrication and performance of mica-based functional membranes. **A)** Schematic representation of 2D muscovite preparation. **B)** XRD pattern and SEM image of OTA-M750. Adapted with permission from reference 17, copyright 2015 RSC Publishing. **C)** Schematic illustration showing the exfoliation process of natural ground mica into eMica nanosheets via intercalation with CTAB. PEI-eMica nanosheets were further mixed with CS solution to produce polymeric mica film by a spray-coating method. **D)** Photograph and cross-sectional SEM image (scale bar, 2  $\mu\text{m}$ ) of a 60 wt.% polymeric mica film. **E)** Schematic illustration of the device with 60 wt.% polymeric mica film as its substrate. **F)**  $I$ - $V$  curves of the device measured in the dark and upon light illumination (450 nm, 180  $\text{mW cm}^{-2}$ , flat and bent). **G)** Time response spectrum of the device to pulsed light at  $V = 1 \text{ V}$ . Adapted with permission from reference 18, copyright 2018 Springer Nature.

The exfoliation of high-quality montmorillonite is relatively easy compared to micas because of their loosely held cation and swelling property. Therefore, montmorillonite films are generally produced through simple dispersion and vacuum filtration. Also, the considerable interlayer distance can serve as molecular separation filters or even ionic transport when tuned.

Huang et al. reported a novel 2D layered membrane based on montmorillonite (MMT) nanosheets prepared by vacuum filtration

on Nylon substrates (Figures 5A and 5B).<sup>20</sup> The two-dimensional MMT membrane showed excellent water permeability ( $212.2 \text{ L/m}^2 \text{ h bar}$ ) and a high rejection rate (95.6%) for DB38 dye molecules (Figure 5C). Besides, the nanochannels in the MMT membrane and wrinkles on MMT nanosheets are rigid enough to resist external pressure up to 0.35 MPa. The lamellar MMT membrane also possessed outstanding hydrophilicity and excellent antifouling property, with an FRR of 88.2% (Figure 5D).

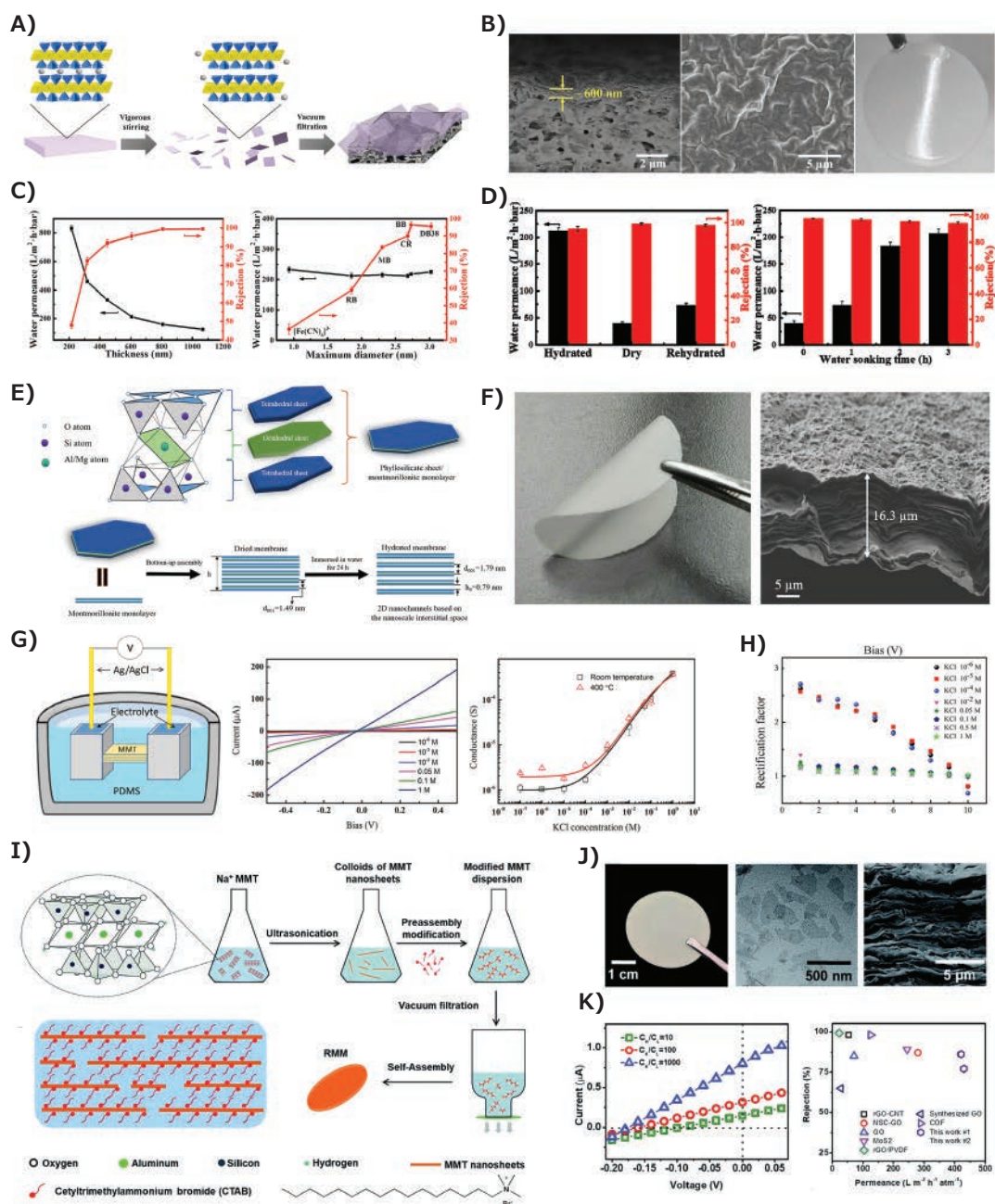


**Figure 5.** Fabrication and performance of smectite-based functional membranes. **A)** Preparation of 2D MMT membrane. **B)** SEM image of MMT membrane surface, cross-section, and digital photograph of MMT membrane. **C)** Separation performances of hydrated lamellar MMT membrane using dead-end filtration. **D)** Effect of membrane hydration on the separation performance of MMT membrane. Adapted with permission from reference 20, copyright 2020 Elsevier. **E)** Structure diagram of MMT crystal and schematic illustration of the construction of the 2D nanochannel arrays based on the lamellar MMT membrane. **F)** Digital photo MMT membrane and cross-sectional SEM image. **G)** Schematic diagram of the 2D nanofluidic device with representative  $I$ - $V$  plots of the 2D nanofluidic device under different concentrations of KCl aqueous solution at room temperature and ionic conductance versus KCl concentration. **H)** Rectification factor as a function of applied bias at KCl electrolyte of various concentrations. Adapted with permission from reference 21, copyright 2018 American Chemical Society. **I)** Fabrication of the reconstructed MMT membrane (RMM). **J)** TEM image, digital photograph, and cross-sectional SEM image of an RMM. **K)** Power generation and permeance/rejection comparison of the RMM. Adapted with permission from reference 22, copyright 2019 Royal Society of Chemistry.



Liu et al. made two-dimensional nanochannel arrays based on a flexible MMT membrane with well-stacked monolayers. They observed the ion transport behavior within the nanochannels (Figure 5E and 5F).<sup>21</sup> Current increases linearly with the bias, and the slope of these  $I$ - $V$  curves corresponds to the ionic conductance inside the 2D nanochannels. Moreover, the ionic conductance began to deviate from the linear relationship at  $10^{-4}$  M. The ionic transport behavior indicates that the electrolyte ion migrates freely inside the two-dimensional nanochannels above  $10^{-4}$  M, but the surface-charge-controlled ionic conductance is dominant below  $10^{-4}$  M (Figure 5G). The surface charge density of the nanochannels is determined to be  $\sim 0.0077$  mC m<sup>-2</sup>, and the ionic mobility ratio ( $\mu_+/ \mu_-$ ) through the 2D nanochannels is calculated to be about 8.2 for KCl electrolyte solution. The asymmetric nanofluidic diode showed ionic current rectification with a rectification factor of  $\sim 2.6$  for the KCl electrolyte (Figure 5H).

Zhou et al. succeeded in fabricating a CTAB-modified MMT membrane (Figures 5I and 5J).<sup>22</sup> The CTAB attached on both sides of the negatively charged MMT nanosheets supported the nanochannels as pillars and played a significant role in capturing dye molecules. The membrane showed high stability in water under soaking, shacking, and short ultrasonication conditions. Not only that, but it could also be used for salinity gradient energy conversion. An output power density of 0.18 W m<sup>-2</sup> was achieved under a 1000-fold salt concentration gradient with a membrane thickness of 11.2  $\mu$ m (Figure 5K). These membranes also showed water permeance of 429 L m<sup>-2</sup> h<sup>-1</sup> atm<sup>-1</sup> with a thickness of 2.5  $\mu$ m, higher than other membranes with the same thickness. They also show high separation efficiency for both positive and negative dyes. The hydroxyl groups on the edge of MMT nanosheets are hydrophilic, while the nanochannels are hydrophobic; the alternating hydrophobic and hydrophilic nanochannels can further promote the permeance. The combination of nanofluidic ionic transport and molecular separation through 2D channels presents valuable features to create new smart multifunctional membranes that can collect energy while purifying wastewater.

## Vermiculite Group

Vermiculites are generally trioctahedral and are termed based on a negative layer charge between 0.5 and 0.9. They are formed mainly by removing potassium from biotite, phlogopite or muscovite, which is why their chemistry is closely linked to mica.<sup>11</sup>

The vermiculite structure contains interlamellar water layers, which are subjected to the hydration and dehydration processes. The type of interlayer cation controls its hydration properties. The smaller or lower the charge of the cation, the larger the interlayer space becomes. These counter cations confined in the adjacent vermiculite layers feature ultra-high intrinsic ion conductivity. Vermiculite can be easily exfoliated in water by an ion-exchange method, which is much greener and more facile than the chemical exfoliation method commonly used for graphene oxides or Mxenes.<sup>10</sup>

Shao et al. produced a self-standing vermiculite film by restacking exfoliated vermiculite sheets (Figure 6A–C).<sup>23</sup> Ionic exchange methods were adopted for fabrication similar to that of other swelling clays. The surface charge density on the vermiculite walls and proton mobility were determined to be around 1.4 mC m<sup>-2</sup> and  $1.2 \times 10^{-3}$  cm<sup>2</sup> V<sup>-1</sup> s<sup>-1</sup>, comparable to that of commercial proton conductor Nafion (Figure 6D and 6E). The produced films had extraordinary thermal stability and maintained swelling properties even after annealing in air at elevated temperatures.

Recently, Cao et al. successfully produced a vermiculite lamellar membrane with a two-dimensional nanofluidic channel with outstanding performance in nanofluidic osmotic energy conversion.<sup>24</sup> The fabrication process was the same, except they used HCl solution to make in-plane nanopores on vermiculite nanosheets to decrease tortuosity and offer additional vertical ion pathways (Figure 6F and 6G). The porous vermiculite membrane achieved a maximum power density of 10.9 W m<sup>-2</sup> at a 1000-fold salinity gradient, outperforming most self-standing phyllosilicate-based 2D lamellar membranes (Figure 6H). The high layer charge compared to smectites and easier exfoliation of nanosheets compared to that of micas gave vermiculites the advantages of being used for building materials for clay-based nanofluidic membranes with high performance. The excellent osmotic energy conversion performance of the porous vermiculite membrane is attributed to the low resistance horizontal and vertical ion transport pathways that facilitate the ion flux. (Figure 6I).

## Conclusion

In this review, we have discussed shortly the applications of 1:1 and 2:1 phyllosilicate material in membrane technology, as well as the basic geometric understanding of their layered structures. Clay minerals have unique properties that allow them to be used suitably for building blocks of laminar membranes with or without chemical modification. Understanding the physical and chemical properties of phyllosilicate materials can help us further develop insights into their possible applications.

## Acknowledgements

This work was supported by the Technology Innovation Programme (20012430) funded by the Ministry of Trade, Industry & Energy (MOTIE, Korea).

## Author Contributions

H. R. conducted research, analyzed the data, and contributed to writing the paper. W.S. conceived, directed, and supervised the research and contributed to writing the paper. S. K., T. K., J. B., H. K., and J. Y. supported research and data analysis. All authors commented on the manuscript.

## Competing Interests

The authors declare no competing interests.

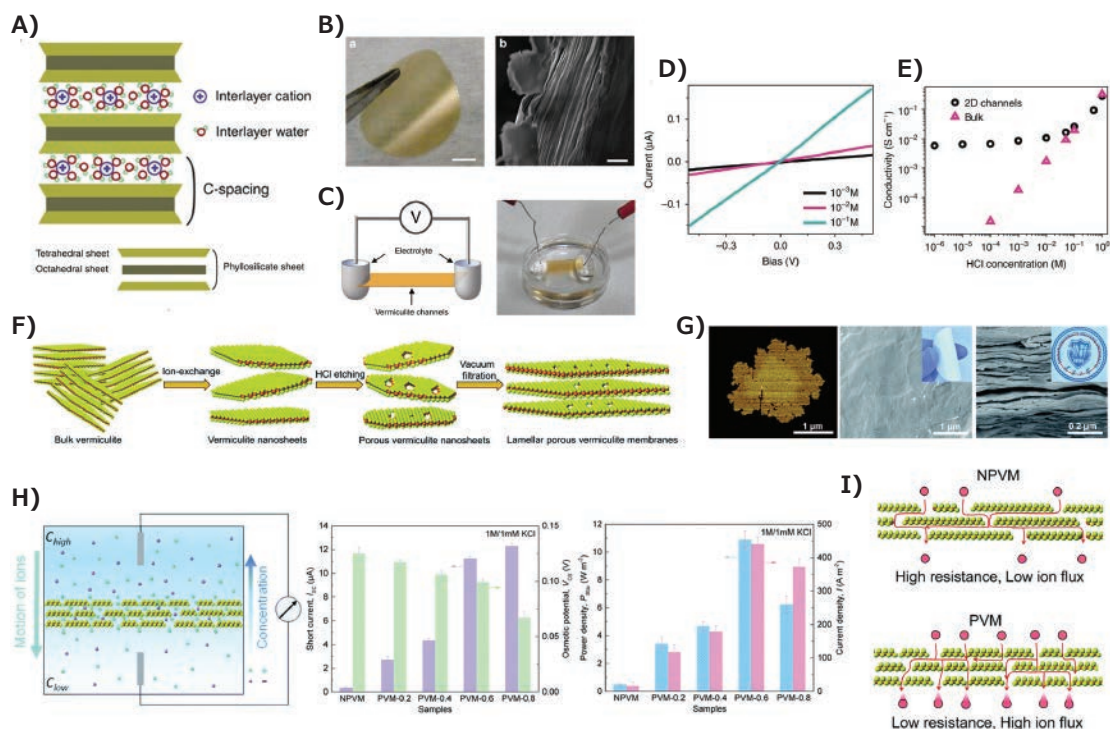


**Figure 6.** Fabrication and performance of nanofluidic vermiculite membranes. **A)** Structural model of vermiculite layers. **B)** A flexible free-standing vermiculite membrane and the cross-sectional SEM image. **C)** Schematic illustration and digital photo of the vermiculite nanofluidic device. **D)** Representative *I-V* curves through the 2D channels. **E)** Ionic conductivity as a function of electrolyte concentration. Adapted with permission from reference 23, copyright 2015 Springer Nature. **F)** Preparation and characterization of porous vermiculite (PV) nanosheets and lamellar membranes (PVM). **G)** AFM image of PV nanosheets, SEM image of PVMs, and SEM image of microporous PES support. **H)** Schematic representation of the experimental set-up, and plot of the generated osmotic potential and power density. **I)** Schematic illustration highlighting the pathways of the lowest resistance of ion transport in a PVM, generating a high flux, while the highly tortuous pathways in a NPVM lead to a high resistance and low ion flux. Adapted with permission from reference 24, copyright 2021 Royal Society of Chemistry.

## Reference

- Stankov, S.; Dikin, D. A.; Dommett, G. H. B.; Kohlhaas, K. M.; Zimney, E. J.; Stach, E. A.; Piner, R. D.; Nguyen, S. T.; Ruoff, R. S. *Nature* **2006**, *442* (7100), 282–86. DOI: 10.1038/nature04969.
- Wehling, T. O.; Novoselov, K. S.; Morozov, S. V.; Vdovin, E. E.; Katsnelson, M. I.; Geim, A. K.; Lichtenstein, A. I. *Nano Lett.* **2008**, *8* (1), 173–77. DOI: 10.1021/nl072364w.
- Wang, Q. H.; Kalantar-Zadeh, K.; Kis, A.; Coleman, J. N.; Strano, M. S. *Nat. Nanotechnol.* **2012**, *7* (11), 699–712. DOI: 10.1038/nnano.2012.193.
- Xu, M.; Liang, T.; Shi, M.; Chen, H. *Chem. Rev.* **2013**, *113* (5), 3766–3798. DOI:10.1021/cr300263a.
- Zhang, Y.; Zheng, Y.; Rui, K.; Hng, H. H.; Hippalgaonkar, K.; Xu, J.; Sun, W.; Zhu, J.; Yan, Q.; Huang, W. *Small* **2017**, *13* (28), 1700661. DOI: 10.1002/smll.201700661.
- Park, J.; Das, D.; Ahn, M.; Park, S.; Hur, J.; Jeon, S. *Nano Converg.* **2019**, *6* (1), 32. DOI: 10.1186/s40580-019-0202-5.
- Nicolosi, V.; Chhowalla, M.; Kanatzidis, M. G.; Strano, M. S.; Coleman, J. N. *Sci.* **2013**, *340*, 1226419. DOI: 10.1126/science.1226419.
- Gao, J.; Feng, Y.; Guo, W.; Jiang, L. *Chem. Soc. Rev.* **2017**, *46* (17), 5400–5424. DOI: 10.1039/C7CS00369B.
- Vo, T. S.; Vo, T. T. B. C.; Suk, J. W.; Kim, K. *Nano Converg.* **2020**, *7* (1), 4. DOI:10.1186/s40580-019-0215-0.
- Hussein, M. A.; El-Said, W. A.; Abu-Zied, B. M.; Choi, J.-W. *Nano Converg.* **2020**, *7* (1), 15. DOI:10.1186/s40580-020-00225-8.
- Barton, C. D. **2002**. Clay Minerals. In: Rattan Lal, comp., ed. Encyclopedia of Soil Science. New York, New York: Marcel Dekker: 187–192.
- B. Velde. **1992** Introduction to Clay Minerals: Chemistry, Origins, Uses and Environmental Significance; Springer:Springer Dordrecht.
- Li, X.; Liu, Q.; Cheng, H.; Zhang, S.; Frost, R. L. *J. Colloid Interf. Sci.* **2015**, *444*, 74–80. DOI: 10.1016/j.jcis.2014.12.039.
- Zhou, Q.; Fu, Y.; Zhang, X.; Luo, T.; Luo, W. *Mat. Sci. Eng. B* **2018**, *227*, 89–99. DOI: 10.1016/j.mseb.2017.10.013.
- Cheng, H.; Zhou, Y.; Feng, Y.; Geng, W.; Liu, Q.; Guo, W.; Jiang, L. *Adv. Mater.* **2017**, *29*, 1700177. DOI: 10.1002/adma.201700177.
- Popper, P. *Nature* **1951**, *168*, 1119–1120. DOI: 10.1038/1681119b0.
- Jia, F.; Song, S. *RSC Adv.* **2015**, *5* (65), 52882–52887. DOI: 10.1039/C5RA07749D.
- Pan, X.-F.; Gao, H.-L.; Lu, Y.; Wu, C.-Y.; Wu, Y.-D.; Wang, X.-Y.; Pan, Z.-Q.; et al. *Nat. Commun.* **2018**, *9*, 2974. DOI: 10.1038/s41467-018-05355-6.
- Odom, I. E. **1984**. Smectite clay Minerals: Properties and Uses. Philosophical Transactions of the Royal Society of London. Series A, Mathematical and Physical Sciences, *311* (1517), 391–409.
- Huang, M.-Y.; Chen, Y.; Yan, X.; Guo, X.-J.; Dong, L.; Lang, W.-Z. *J. Membr. Sci.* **2020**, *614*, 118540. DOI: 10.1016/j.memsci.2020.118540.
- Liu, M.-L.; Huang, M.; Tian, L.-Y.; Zhao, L.-H.; Ding, B.; Kong, D.-B.; Yang, Q.-H.; Shao, J.-J. *ACS Appl. Mater. Interfaces* **2018**, *10* (51), 44915–44923. DOI: 10.1021/acsami.8b17719.
- Zhou, Y.; Ding, H.; Smith, A. T.; Jia, X.; Chen, S.; Liu, L.; Chavez, S. E.; et al. *J. Mater. Chem. A* **2019**, *7* (23), 14089–14096. DOI: 10.1039/C9TA00801B.
- Shao, J.-J.; Raidongia, K.; Koltonow, A. R.; Huang, J. *Nat. Commun.* **2015**, *6* (1), 7602. DOI: 10.1038/ncomms7602.
- Cao, L.; Wu, H.; Fan, C.; Zhang, Z.; Shi, B.; Yang, P.; Qiu, M.; Khan, N. A.; Jiang, Z. *J. Mater. Chem. A* **2021**, *9* (25), 14576–14581. DOI: 10.1039/D1TA02400K.



## Nanoclays

Name	Form	Particle Size (µm)	Cat. No
Halloysite nanoclay	powder	30-70 nm × 1-3 µm, nanotube	685445-100G 685445-500G
Nanoclay, hydrophilic bentonite	powder	≤25	682659-500G
Nanoclay, surface modified	powder	≤20	682632-500G
Nanoclay, surface modified	powder	≤20	682608-500G
	powder	≤20	682624-500G

## Polyacrylic Acid

Average Molecular Weight	Viscosity / Concentration	Cat. No
M <sub>w</sub> 1800	≤2000 cP	323667-5G 323667-100G 323667-250G
M <sub>w</sub> ~2,000	50 wt. % in H2O	535931-100G
M <sub>w</sub> ~100,000	35 wt. % in H2O	523925-100ML 523925-500ML
M <sub>n</sub> 130,000 (Typical)		181293-10G
M <sub>w</sub> ~250,000	35 wt. % in H2O	416002-5ML 416002-250ML 416002-500ML
M <sub>v</sub> ~450,000	350-2500 cP	181285-5G 181285-100G 181285-250G
M <sub>v</sub> ~1,250,000	800-11,000 cP	306215-5G 306215-100G 306215-250G
M <sub>v</sub> ~3,000,000	30,000-40,000 cP	306223-100G 306223-250G
M <sub>v</sub> ~4,000,000	40,000-60,000 cP	306231-5G 306231-100G

## Other Phyllosilicates

Name	Form	Size	Description	Cat. No
Kaolinite	powder	-		03584-250G 03584-1KG
Sepiolite	powder	-	<=10% loss on drying	70253-1KG
Montmorillonite	powder	-	surface area: 250 m2/g	69866-100G 69866-1KG
Muscovite Mica for AFM	solid	15 mm x 15 mm x 0.15-0.2 mm	pack of 10	AFM-71855-15-10
	solid	"diameter: 12 mm thickness: 0.15-0.2 mm"	pack of 10	AFM-71856-02
	solid	"diameter: 15 mm thickness: 0.15-0.2 mm"	pack of 10	AFM-71856-03



MERCK

# subscribe today

Don't miss another topically focused technical review.

It's **free** to sign up for a print or digital subscription of *Material Matters*™.

- Advances in cutting-edge materials
- Technical reviews on emerging technology from leading scientists
- Peer-recommended materials with application notes
- Product and service recommendations



To view the library of past issues or to subscribe, visit: [SigmaAldrich.com/mm](http://SigmaAldrich.com/mm)

Merck KGaA  
Frankfurter Strasse 250  
64293 Darmstadt, Germany

MERCK

Exceptional variety.  
Quick delivery.

# NOW!

All you need to keep your discoveries moving forward. Breakthrough ideas require access to the basics. That's why we remain committed to providing you with an unmatched chemical and biochemical portfolio, in with many products shipping the same day your order is placed.

Visit, [SigmaAldrich.com/matsci](https://www.sigmaaldrich.com/matsci)  
to order **SCIENCESATIONAL**



© 2022 Merck KGaA, Darmstadt, Germany and/or its affiliates. All Rights Reserved. Merck, Material Matters, the vibrant M, and Sigma-Aldrich are trademarks of Merck KGaA, Darmstadt, Germany or its affiliates. All other trademarks are the property of their respective owners. Detailed information on trademarks is available via publicly accessible resources.  
Lit. No. MK\_BR9785EN



The life science business of Merck operates as MilliporeSigma in the U.S. and Canada.

**Sigma-Aldrich®**  
Lab & Production Materials